Cellular/Molecular

Nanoscale Phosphoinositide Distribution on Cell Membranes of Mouse Cerebellar Neurons

Kohgaku Eguchi, Elodie Le Monnier, and Ryuichi Shigemoto

Institute of Science and Technology Austria (ISTA), Am Campus 1, Klosterneuburg 3400, Austria

Phosphatidylinositol-4,5-bisphosphate ($PI(4,5)P_2$) plays an essential role in neuronal activities through interaction with various proteins involved in signaling at membranes. However, the distribution pattern of $PI(4,5)P_2$ and the association with these proteins on the neuronal cell membranes remain elusive. In this study, we established a method for visualizing $PI(4,5)P_2$ by SDS-digested freeze-fracture replica labeling (SDS-FRL) to investigate the quantitative nanoscale distribution of $PI(4,5)P_2$ in cryo-fixed brain. We demonstrate that $PI(4,5)P_2$ forms tiny clusters with a mean size of ~1000 nm^2 rather than randomly distributed in cerebellar neuronal membranes in male C57BL/6J mice. These clusters show preferential accumulation in specific membrane compartments of different cell types, in particular, in Purkinje cell (PC) spines and granule cell (GC) presynaptic active zones. Furthermore, we revealed extensive association of $PI(4,5)P_2$ with $Ca_V2.1$ and GIRK3 across different membrane compartments, whereas its association with mGluR1α was compartment specific. These results suggest that our SDS-FRL method provides valuable insights into the physiological functions of $PI(4,5)P_2$ in neurons.

Significance Statement

In this study, we established an electron microscopic method to visualize and analyze the quantitative distribution pattern of phosphatidylinositol-4,5-bisphosphate ($PI(4,5)P_2$) on cell membranes using cryo-fixed brain tissues and SDS-digested freeze-fracture replica labeling. $PI(4,5)P_2$ interacts with various ion channels and receptors to regulate membrane signaling but its nanoscale distribution and association with these proteins remain elusive. This method revealed $PI(4,5)P_2$ clusters preferentially accumulated in specific membrane compartments and its distinct associations with $Ca_V2.1$, GIRK3, and mGluR1α in the mouse cerebellum. These results demonstrate usefulness of the method for gaining insights into the physiological functions of $PI(4,5)P_2$.

Introduction

Phosphoinositides (PIs) are minor components on the cytoplasmic side of eukaryotic cell membranes, but they play essential

roles in a wide variety of cellular functions. In neuronal cells, each stereoisomer of PIs is distributed in different subcellular compartments (Wenk and De Camilli, 2004; Haucke, 2005; Idevall-Hagren and De Camilli, 2015): PI(4)P is enriched in the membrane of the Golgi apparatus and synaptic vesicles (SVs), $PI(4,5)P_2$ and $PI(3,4,5)P_3$ mainly exist in the plasma membrane, PI(3)P and $PI(3,5)P_2$ are selectively concentrated on early and late endosomes, respectively. PIs contribute to various aspects of neuronal activity, such as synaptic transmission and maintenance of membrane excitability by regulating ion channels and intracellular signaling pathways. At chemical synapses, PIs regulate exocytosis and endocytosis of synaptic vesicles at the presynaptic sites (T.F.J. Martin, 2001; Ueda and Hayashi, 2013; Posor et al., 2015; Lei et al., 2017). Many presynaptic proteins involved in such regulation have binding domains to stereoisomers of PIs (Di Paolo and De Camilli, 2006; Falkenburger et al., 2010), indicating their potential role as an anchor for these proteins to regulate their localization and dynamics during synaptic transmission. At the postsynaptic sites, PIs regulate plasticity of dendritic spines through actin remodeling during long-term potentiation (T.F.J. Martin, 2001; Ueda and Hayashi, 2013; Posor et al., 2015; Lei et al., 2017).

Table 1. Antibody list for SDS-FRL

Molecule	Catalog #	Host	Supplier	Epitope	RRID	Lot	Conc.	Specificity	Reference
GST	A190-122A	Rb	Bethyl	—	AB_67419	#11	5 µg/ml	W/o antigen	Present study
GST	A190-123A	Ck	Bethyl	—	AB_66670	#2	5 µg/ml	W/o antigen	Present study
RFP	M155-3	Ms	MBL	—	AB_1278880	#016	2 µg/ml	W/o antigen	Present study
$Ca_V2.1$	152 205	Gp	SYSY	Rt 1921-2212aa	AB_2619842	#1–5	2.5 µg/ml	KO, FRL	Eguchi et al. (2022)
GluD2	MSFR102610	Gp	FI	Ms 897-934aa	AB_2571603	—	2 µg/ml	KO, IF	Konno et al. (2014)
GIRK3	MSFR102100	Rb	FI	Ms 358-389aa	AB_2571714	—	4 µg/ml	KO, FRL	Luján et al. (2018b)
$mGluR1\alpha$	MSFR104080	Gp	FI	Ms 945-1127aa	AB_2571801	—	2 µg/ml	KO, FRL	Mansouri et al. (2015)

Rb, rabbit; Ck, chicken; Ms, mouse; Gp, guinea pig; Rt, rat; SYSY, Synaptic Systems; FI, Frontier Institute; KO, knock-out; FRL, SDS-digested freeze-fracture replica labeling; IF, immunofluorescence; -, information is not provided by suppliers.

The distribution pattern of PIs and their association with signaling proteins at neuronal cell membranes are crucial for understanding their roles in neuronal activities, but have been poorly investigated because of several technical issues with the conventional methods (Tsuji et al., 2019). For example, immunostaining with an anti-PI(4,5)P_2 antibody in aldehyde-fixed cell preparations may not show actual phospholipid distribution because aldehydes cannot fix the lateral diffusion of most membrane lipids (K.A.K. Tanaka et al., 2010). For live cell imaging of PIs, fluorescent protein tagged PI-binding domain (PBD) has been used as specific PI probes (Maekawa and Fairn, 2014; Idevall-Hagren and De Camilli, 2015). However, this method has insufficient spatial resolution to observe the nanoscale PIs distribution in small membrane compartments, such as presynaptic active zones (AZs) and postsynaptic densities (PSDs). In addition, the overexpressed PBD-based probes mask PIs and competitively interfere with their interactions with proteins (Suh and Hille, 2008).

To solve these issues and visualize the nanoscale distribution of PIs on cell membranes, sodium dodecyl sulfate-digested freeze-fracture replica labeling (SDS-FRL) combined with cryofixation has been used (Fujita et al., 2009; Ozato-Sakurai et al., 2011; Cheng et al., 2014; Aktar et al., 2017; Tsuji et al., 2019). This electron microscopic method enables nanoscale phospholipid visualization with physically fixed PIs by high-pressure freezing and carbon/platinum replication. In this study, we optimized this SDS-FRL method and investigated the nanoscale distribution of PI(4,5)P_2 on mouse cerebellar neuronal membranes using recombinant GST-tagged pleckstrin homology (PH) domain of phospholipase Cδ1 (PLCδ1) as a specific PI(4,5)P_2 probe. This approach allowed us to examine the numbers, densities, and distribution patterns of PI(4,5)P_2 on somatodendritic and axonal membranes, including postsynaptic and presynaptic sites. We show that PI(4,5)P_2 makes small clusters on neuronal membranes and specifically co-clusters with P/Q-type voltage-gated calcium channels, G-protein-coupled inwardly rectifying potassium channels, and metabotropic glutamate receptors in distinct membrane compartments, giving insights into the physiological functions of PI(4,5)P_2 in the regulation of neuronal excitability and neurotransmitter release.

Materials and Methods

Animals
Animal experiments were conducted in accordance with the guideline of the Institute of Science and Technology Austria (Animal license number: BMWFW-66.018/0012-WF/V/3b/2016). Male C57BL/6J (stock #000664) mice at postnatal (P) five to seven weeks were used in this study. Mice were initially purchased from The Jackson Laboratory and were bred at the Preclinical Facility of IST Austria on 12/12 h light/dark cycle with access to food and water *ad libitum*. All experiments were performed in the light phase of the cycle.

Antibodies
Table 1 shows a list of the primary antibodies containing their epitopes, concentrations for use, suppliers, and specification that were used in this study. Gold particle-conjugated secondary antibodies were purchased from British Biocell International (BBI, goat anti-rabbit IgG, 5 nm; goat anti-guinea pig IgG, 10 nm; goat anti-mouse IgG, 15 nm) and Jackson ImmunoResearch (donkey anti-chicken IgY, 6 nm; donkey anti-guinea pig IgG, 12 nm).

Liposome preparation and high-pressure freezing
Phosphatidylcholine (18:1 (Δ9-Cis) PC), phosphatidylethanolamine (18:1 (Δ9-Cis) PE), phosphatidylserine (18:1 (Δ9-Cis) PS), phosphatidylinositol (18:1 PI), and phosphoinositides (18:1) were purchased from Avanti Polar Lipids. All liposomes contained 45 mol % PC, 30 mol % PE, 20 mol % PS, and either 5 mol % PI or a phosphoinositide. When preparing liposomes containing various concentration of PI(4,5)P_2, the total concentration of PC and PI(4,5)P_2 was adjusted to 50 mol%. Solutions of PC, PE, and PS in chloroform and PI or phosphoinositides in chloroform:methanol:H_2O:HCl (1 N; 20:9:1:0.1) were mixed in the required proportion in amber-color glass vials. To improve phosphoinositide homogenization with other lipids, the chloroform:methanol 2:1 ratio was maintained in the mixture. A lipid film was produced by evaporation of solvents in the vial under the stream of nitrogen gas and then drying using a vacuum desiccator for 2 h. The dried lipid film was stored at $-20°C$ with argon gas and used within 2 d.

The lipid film was resuspended in a buffer containing 220 mM sucrose and 20 mM HEPES (pH 7.4, adjusted with NaOH). The suspension was vortexed well and then freeze-thawed 5 times in liquid nitrogen and warm water (~60°C). Unilamellar liposomes were produced by extrusion through a 0.4-µm pore size polycarbonate filter using an extrusion apparatus (Avanti Polar Lipids). After extrusion, the liposomes were diluted five times in 120 mM NaCl, 20 mM HEPES buffer (pH 7.4, adjusted with NaOH), and centrifuged for 10 min at $10,000 \times g$. The supernatant was carefully removed, and glycerol was applied as a cryoprotectant to the liposome pellet to a final concentration of 50%. The liposome/glycerol mixture was placed on a copper carrier with a ring of double-sided tape (140-µm thickness), covered with another carrier, and then frozen by a high-pressure freezing machine (HPM010, BAL-TEC). The frozen samples were stored in liquid nitrogen until use.

Cell culture, transfection, and high-pressure freezing of HEK293 cells
The cDNA pCAGG PM-FRB-mRFP-T2A-FKBR-5-ptase was constructed by adding the PM-FRB-mRFP-T2A-FKBP-5-ptase fragment (a gift from Peter Varnai, Addgene, #40896; http://n2t.net/addgene:40896; RRID:Addgene_40896; Tóth et al., 2012) to pCAGG vector from our own library. Plasmid DNA was purified on a Nucleobond AX anionexchange column (Macherey-Nagal).

Human Embryonic kidney 293 (HEK293) cells were seeded at a density of 2×10^6 cells per 100-mm dish and maintained in DMEM supplemented with 10% fetal bovine serum, 100 U/ml penicillin and streptomycin (Invitrogen) in a humidified atmosphere (5% CO_2) at 37°C. HEK293 cells were transiently transfected using Lipofectamine 3000 (ThermoFisher Scientific) according to the manufacturer's protocol. Forty-eight hours after transfection, cells were treated with 0.25% trypsin-EDTA (Sigma-Aldrich) for 2–5 min at 37°C and collected by centrifugation ($100 \times g$, 5 min). After removing supernatant, cells were

incubated with rapamycin (5 μM with 0.1% DMSO) or 0.1% DMSO dissolved in PBS for 5 min at room temperature (RT) and centrifuged for 5 min at 100 × g. The supernatant was carefully removed, and the pellet was placed on a copper carrier with a ring of double-sided tape (140-μm thickness), covered with another carrier, and then frozen by a high-pressure freezing machine. The frozen samples were stored in liquid nitrogen until use.

High-pressure freezing of acute cerebellar slices
Acute slices of mouse cerebellum were prepared at physiological temperature (PT) to avoid the alternation of the neuronal conditions, such as profound loss of dendritic spines and synaptic proteins, as described previously (Eguchi et al., 2020). Briefly, mice were decapitated under isoflurane anesthesia and their brains were quickly removed from the skull and immersed into a cutting solution containing (mM): 300 sucrose, 2.5 KCl, 10 glucose, 1.25 NaH$_2$PO$_4$, 2 Na Pyruvate, three *myo*-inositol, 0.5 Na ascorbate, 26 NaHCO$_3$, 0.1 CaCl$_2$, 6 MgCl$_2$ (pH 7.4 when gassed with 95% O$_2$/5% CO$_2$) at PT (35–37°C). The cerebellum was dissected from the whole brain and immediately glued on a cutting stage of a tissue slicer (Linear Slicer Pro7, Dosaka EM) and sliced (sagittal, 140–160 μm thickness) in the cutting solution kept at PT. Slices were then maintained in the artificial cerebrospinal fluid (ACSF) containing (in mM): 125 NaCl, 2.5 KCl, 10 glucose, 1.25 NaH$_2$PO$_4$, 2 sodium pyruvate, three *myo*-inositol, 0.5 sodium ascorbate, 26 NaHCO$_3$, 2 CaCl$_2$, 1 MgCl$_2$ (pH 7.4 when gassed with 95% O$_2$/5% CO$_2$) at 37°C until use. Small blocks containing lobule IV–VII were trimmed from the slices in the cutting solution using a micro scalpel (#10316-14, FST) and transferred into cryoprotectant buffer [15% polyvinylpyrrolidone (PVP) in ACSF with 10 mM HEPES, pH 7.3 adjusted with NaOH], sandwiched between two copper carriers with a ring of double-sided tape (140-μm thickness), and then frozen by a high-pressure freezing machine. The frozen samples were stored in liquid nitrogen until use. We froze the acute cerebellar slices within 2 h after slicing to ensure that the slice condition did not alter (Eguchi et al., 2020).

SDS-digested freeze-fracture replica labeling (SDS-FRL)
The frozen samples were fractured into two parts at −130°C and replicated by carbon (4–5 nm thick), carbon-platinum (uni-direction from 60°, 2 nm), and carbon (20–25 nm) deposition in a freeze-fracture machine (JFD-V, JOEL). The samples were digested with 2.5% SDS in 0.1 M Tris-HCl (pH 8.3) at 80°C for 18–22 h. The replicas were washed in the SDS solution and then a washing buffer (50 mM Tris-buffered saline (TBS; pH 7.4) containing 0.1% BSA) at RT. To avoid nonspecific binding of the probes and antibodies, the replicas were blocked with 3% BSA, 2% cold fish skin gelatin, and 0.05% Tween 20 in TBS for 1 h at RT. The replicas were incubated with 50 ng/ml GST-tagged PH domain of phospholipase C δ1 (PI(4,5)P$_2$-Grip, Echelon Inc.) in a dilution buffer (1% BSA, 1% cold fish skin gelatin, and 0.05% Tween 20 in TBS) at 4°C overnight. Then the replica was incubated with anti-GST antibody and anti-Ca$_V$2.1 antibody as a marker of neurons at 15°C overnight, and then gold-nanoparticle conjugated secondary antibodies dissolved in the dilution buffer at 15°C overnight. For double labeling of PI(4,5)P$_2$ with proteins, the replicas were incubated with a mixture of primary antibodies (GluD2: rabbit anti-GST + guinea pig anti-GluD2; GIRK3: chicken anti-GST + rabbit anti-GIRK3; mGluR1α: rabbit anti-GST + guinea pig anti-mGluR1α) at 15°C 1–2 overnight and then with gold-nanoparticle conjugated secondary antibodies at 15°C overnight. After washing the replicas with the washing buffer, they were picked up onto a grid coated with formvar in distilled water. Images were obtained under TEM (Tecnai 10) operated at 80 kV with RADIUS software at magnifications of 65,000 and 39,000.

Image analysis
Images were analyzed with Darea software (Kleindienst et al., 2020), Fiji (Schindelin et al., 2012), and R. The gold particle detection and the demarcation of the region of interest were performed on Darea software. AZs on the P-face of PF boutons were indicated with the aggregation of intramembrane particles on the replica at the electron microscopic level as described previously (Landis and Reese, 1974; Harris and Landis,

1986; Masugi-Tokita et al., 2007; Eguchi et al., 2020, 2022). Gold particles inside or <30 nm away from the demarcation border of AZs (outer rim) were counted as the particles in the AZs (Kleindienst et al., 2020). Because the PSD area on the P-face of dendritic spines of PCs cannot be identified based on morphologic features, the largest cluster of GluD2-labeling gold particles on the spines was identified as the PSD area (Konno et al., 2014; Luján et al., 2018a; Eguchi et al., 2020). The demarcated region of the images was imported to R via FIJI/ImageJ for the following point pattern analysis.

Point pattern analysis of the gold particles described below was performed using spatstat package (version 2.3–0) of R (version 4.1.0). Nearest neighbor distances (NNDs) to both particles of the same size (e.g., from a 5-nm particle to the nearest 5-nm particle) and the other size (e.g., from a 5-nm particle to the nearest 10-nm particle) were computed to evaluate the distribution pattern of the particles. Center Periphery Index (CPI), indicating the location of the particles in the AZs or PSDs, was calculated as the square of the normalized distances from the center of the region of interest. When particles are randomly distributed in a circle, the mean CPI is near 0.5 (Kleindienst et al., 2020). To assess the randomness of the particle distribution, we performed two types of Monte-Carlo simulations, termed random and fitted simulations, following the methods described in the previous publications (Luján et al., 2018b; Kleindienst et al., 2020) using R. For the random simulation, particles were randomly placed on the demarcated area. The simulated particles were placed to keep the minimum distance of 10 nm from any other particles and then randomly shifted within a disk with a 30-nm diameter to reproduce the immunolabeling with a probe and antibodies (Tabata et al., 2019). In the fitted simulation, a constraint was added that the distance distribution between the simulated particles should not differ significantly from the distance distribution between the original particles. The particle distribution pattern was modeled and simulated as a Matern Cluster point process, and the goodness-of-fit between the real and simulated distribution was assessed by comparing both the all pairwise distances (APD) and NNDs of the particles using the two-sample Kolmogorov–Smirnov test (KS test), respectively, and considered them similar if the *p*-value was equal or above 0.1 for both. To avoid excessive statistical power because of the large sample size caused by a large number of particles, parametric bootstrapping was performed when the number of values to be compared exceeded 100. Specifically, we first randomly selected 100 distance values (NND or APD) from the simulated distribution and compared them to the empirical cumulative distribution function of the distance values of the real distribution using the KS test. This process was repeated 1000 times, and the average of the *p*-values was used to assess the goodness-of-fit.

Gold particle clusters were detected with a hierarchical clustering algorithm called Ward linkage and a density-based clustering algorithm called DBSCAN. For Ward linkage, the threshold distance was set as 50 nm. For DBSCAN, we set the minimum number of particles consisting of a cluster as three and the maximum distance between particles as the sum of the median and 1.5 times the interquartile range (IQR) of the NNDs. The area of the convex polygon connecting the outermost particles forming the cluster was defined as the cluster area.

Estimation of the labeling efficiency
The labeling efficiency for PI(4,5)P$_2$ with GST-PH was estimated on liposome replicas containing 0.01–5 mol% PI(4,5)P$_2$. Considering that a single phospholipid molecule occupies a space of ~0.65 nm^2 (Nagle and Tristram-Nagle, 2000), 750,000 phospholipids would construct a half leaflet of a 1 μm^2 lipid bilayer. Background gold particle density (20 particles/μm^2; Fig. 1B) was subtracted from the gold particle density on the liposomes. The labeling efficiency for each PI(4,5)P$_2$ concentration was estimated by dividing the gold particle density by the theoretical PI(4,5)P$_2$ density. For example, a 5 mol% PI(4,5)P$_2$-containing liposome replica has a theoretical density of 37 500 molecules/μm^2, thus the labeling efficiency is estimated to be 2.3% based on the gold particle density of 850 particles/μm^2. Assuming random distribution of PI(4,5)P$_2$ on the liposomes, the expected mean NND ($\overline{NND}$) of the molecules is given as:
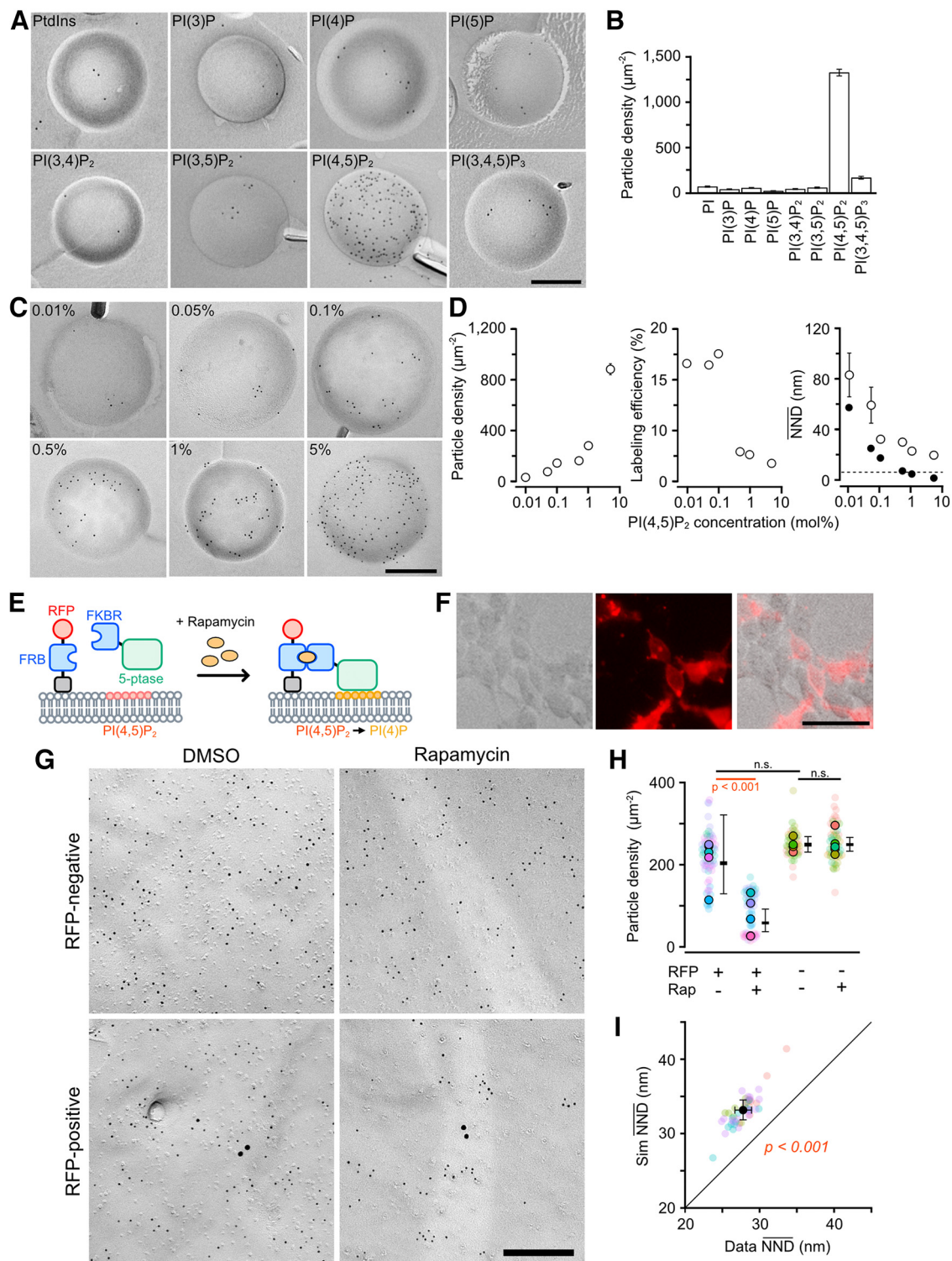
Figure 1. PI(4,5)P$_2$ labeling using SDS-FRL. *A*, Example transmission electron microscopic (TEM) images of liposome replicas containing 5% PtdIns or different stereoisomers of PIs labeled with GST-PH, anti-GST antibody, and 5-nm gold particle-conjugated secondary antibody. Scale bar = 200 nm. *B*, Bar graph indicating the gold particle density on the liposome replicas. The density of gold particles was the highest in the liposome containing PI(4,5)P$_2$. *C*, Example TEM images of liposome replicas containing different concentration of PI(4,5)P$_2$. PI(4,5)P$_2$ was labeled with 5-nm gold particles. Scale bar = 200 nm. *D*, Concentration-dependent changes of the PI(4,5)P$_2$ labeling. Left, The gold particle densities in the liposome replica. Middle, The labeling efficiency for PI(4,5)P$_2$. Right, The mean NNDs of the observed gold particles (open) and theoretical mean NNDs of randomly distributed PI(4,5)P$_2$ molecules (black). Dashed line indicates the diameter of PLCδ1-PH. Error bars indicate SEM. *E*, Schema of chemically-inducible PI(4,5)P$_2$ depletion with FRB-FKBR system. Rapamycin induces heterodimerization of FRB and FKBR, causing translocation of 5-ptase on the cell membrane. *F*, Example image of HEK293 cells transfected with PM-FRB-mRFP-TA-FKBR-5-ptase (left, bright field; middle, mRFP fluorescent; right, merged). Scale bar = 50 μm. *G*, Example TEM images of 5-nm gold particle labeling for PI(4,5)P$_2$ on the P-face of the somatic membranes of HEK293 cells treated with rapamycin (5 μM) or vehicle (0.1% DMSO). The somatic membranes of the transfected cells were identified by immunogold labeling for RFP (15 nm). Scale bar = 200 nm. *H*, Statistical comparison of the PI(4,5)P$_2$ particle density on the somatic membranes of HEK293 cells. Closed and transparent circles indicate the means of PI(4,5)P$_2$ particle density in each cell and each image, respectively, with colors indicating different cells. Horizontal bars and error bars indicate estimated marginal means (emmeans) and 95% confidence intervals (CIs) of the density estimated by GLMM (see Materials and Methods). The density on the rapamycin-treated transfected cells was

$$\overline{NND} = \frac{0.5}{\sqrt{D}}, \tag{1}$$

where D is the density of the molecules in the area.

Statistical analysis
To consider the hierarchical structure, correlation, and probability distribution, data were analyzed with either a linear mixed-effects model (LMM) or its generalized form (GLMM) using the lme4 package (version 1.1–27.1) of R (Aarts et al., 2014; Yu et al., 2022). Probability distributions for models were chosen by the goodness of fit to Poisson (for discrete variables e.g., the number of particles), normal (e.g., CPI), or the gamma distribution (for continuous variables e.g., NNDs). Appropriate to the particular experiment and statistical model, treatments (transfection, rapamycin-application), the faces of cell membranes (P- and E-face), components of neurons (e.g., somata, spines, AZs on PF boutons), and potentially their interactions were used as fixed effects, while experiments, animals, replicas, and cells were used as random effects to consider the nested and/or crossed data structure in the statistical analysis. For all experiments, at least four animals per condition were used. All data are presented as estimated marginal means (emmeans) with 95% confidence intervals (CIs, in figures) or SEM (in text) estimated using the emmeans package. The goodness-of-fit of the models was assessed by second-order Akaike Information Criterion (AICc) for the elimination of the random factors (MuMIn package) and then by likelihood ratio χ^2 tests (Chi-LRT) with models in which the fixed effects of interest had been dropped. For multiple pairwise comparisons between three or more groups, *post hoc* comparisons to assume the significance of differences between pairs of group means were performed using emmeans packages with Tukey (for all pairwise) or Benjamini-Hochberg (BH, for selected pairwise) method when Chi-LRT detected a significant difference ($p < 0.05$). Statistical significance was assumed if $p < 0.05$ (indicated with blue or single asterisk), $p < 0.01$ (green or double asterisk), and $p < 0.001$ (red or triple asterisk).

Results

Visualization of nanoscale PI(4,5)P$_2$ distribution using SDS-digested freeze-fracture replica labeling
To observe the nanoscale two-dimensional (2D) distribution of PI(4,5)P$_2$, SDS-FRL has been used on cultured human fibroblasts, mouse smooth muscle cells, and rat pancreatic exocrine acinar cells (Fujita et al., 2009; Ozato-Sakurai et al., 2011). In this study, we optimized this method for mouse cerebellar tissues to visualize the nanoscale PI(4,5)P$_2$ distribution on neuronal cell membranes. We used a recombinant GST-tagged PH domain of PLCδ1 (GST-PH) as a specific probe of PI(4,5)P$_2$. To verify the specificity of GST-PH among the PI stereoisomers, we labeled freeze-fracture replicas of liposomes containing either PhdIns or a PI stereoisomer (5 mol%) with GST-PH (50 ng/ml), anti-GST primary antibody, and gold particle-conjugated secondary antibody. The density of immunogold particles was much higher on the replica prepared from PI(4,5)P$_2$ liposome compared with those from others (Fig. 1A), indicating a high specificity of the probe for PI(4,5)P$_2$ among PI stereoisomers (Fig. 1B). To assess the labeling efficiency, we labeled PI(4,5)P$_2$ on the liposome replicas containing different concentration of PI(4,5)P$_2$ (Fig. 1C). The particle density increased in a PI(4,5)P$_2$ concentration-

dependent manner (Fig. 1D, left). The labeling efficiency, estimated from the theoretical PI(4,5)P$_2$ molecule density (see Materials and Methods), was ~17% in the range of 0.01–0.1 mol %, while the efficiency drastically dropped to 2–3% for liposomes containing >0.5 mol% PI(4,5)P$_2$ (Fig. 1D, middle). The mean nearest neighbor distances (NNDs) of the gold particles decreased in a PI(4,5)P$_2$-concentration-dependent manner, with a relatively constant NND of ~20 nm for concentrations above 1 mol% (Fig. 1D, right). The mean NNDs for the gold particles were larger than the values calculated from the theoretical PI(4,5)P$_2$ molecule densities at all concentrations. Since the diameter of PLCδ1-PH-Ins(1,4,5)P$_3$ complex has been reported as ~6 nm from the crystal structure analysis (Ferguson et al., 1995), the reduction of the labeling efficiency for PI(4,5)P$_2$ above 0.5 mol% (mean NND for the theoretical PI(4,5)P$_2$ = 8 nm) is probably because of the physical limitation of GST-PH binding to high density PI(4,5)P$_2$. Nonetheless, particle density and mean NNDs in the 0.01–5 mol% range are PI(4,5)P$_2$ concentration-dependent, indicating that quantitative comparison of PI(4,5)P$_2$ distribution pattern is possible.

To evaluate the specificity of GST-PH for PI(4,5)P$_2$ labeling on the cell membrane, we introduced a PI(4,5)P$_2$ depletion system using rapamycin-inducible heterodimerization proteins (PM-FRB-mRFP-T2A-FKBR-5-ptase; Tóth et al., 2012) into HEK293 cells. In this system, membrane anchor domain and 5-phosphatase (5-ptase) are fused to FRB domain of mTOR (FRB) and its binding partner, FK506 binding protein 12 (FKBR), respectively. Rapamycin induces FRB-FKBR heterodimerization, which rapidly translocates 5-ptase to the cell membrane and converts PI(4,5)P$_2$ to PI(4)P (Fig. 1E). By the transfection of the plasmid to HEK293 cells, ~50% of the cells on the dish showed mRFP fluorescence indicating the transfection of the system (Fig. 1F). Cells collected by trypsin treatment and centrifugation were applied with rapamycin or vehicle (DMSO), then frozen under high pressure and labeled with PI(4,5)P$_2$ by SDS-FRL. We labeled RFP with larger gold particles to identify the transfected cells. Although the particle density for RFP was very low because most of the membrane-anchored PM-FRB-mRFP was probably removed by SDS-digestion, we could identify RFP-positive and negative cells from the difference in the RFP-labeling particle density (RFP-positive: 0.44 ± 0.06 particles/μm^2, $n = 10$ cells; RFP-negative: 0.07 ± 0.02 particles/μm^2, $n = 9$ cells; Welch's t test: $p < 0.001$). PI(4,5)P$_2$-labeling gold particles (PI(4,5)P$_2$ particles) were distributed on the cytoplasmic side (P-face) of HEK293 cells (Fig. 1G) and the particle density in the transfected cells applied with rapamycin was significantly lower than in other conditions (multiple pairwise comparisons with Tukey adjustment (Tukey): $p < 0.001$; Fig. 1H). The PI(4,5)P$_2$ molecule density of the transfected/DMSO-applied (control) or/rapamycin-applied (Rap) cells can be estimated to be 4076 and 343 molecules/μm^2, respectively, based on the gold particle densities (control = 203.8 ± 47.3 particles/μm^2, Rap = 58.3 ± 13.6 particles/μm^2; Fig. 1H) and the labeling efficiencies estimated in Figure 1D (control = 5%, Rap = 17%), indicating that PI(4,5)P$_2$ density was reduced ~92% by the application of rapamycin to the transfected cells. These results demonstrate the specificity of the PI(4,5)P$_2$ labeling using SDS-FRL.

To investigate whether PI(4,5)P$_2$ is clustered on HEK293 cell membranes, we performed Monte-Carlo random simulations and compared the NNDs between the observed and simulated PI(4,5)P$_2$ particles from all images (Szoboszlay et al., 2017). The mean NND of the observed PI(4,5)P$_2$ particle distribution was significantly smaller than that of the simulated

←

significantly lower than others. *I*, Comparison of nearest neighbor distances (NND) between real (Data NND, *x*-axis) and simulated (Sim NND, *y*-axis) PI(4,5)P$_2$ particles on the somatic membranes of the untransfected HEK293 cells treated with DMSO. Data-NNDs are significantly smaller than Sim NNDs [Data: 27.8 ± 0.6 nm, Sim: 33.2 ± 0.7 nm, $n = 49$ images/4 cells, $p < 0.001$, likelihood ratio χ^2 test (Chi-LRT)]. n.s., not significant.
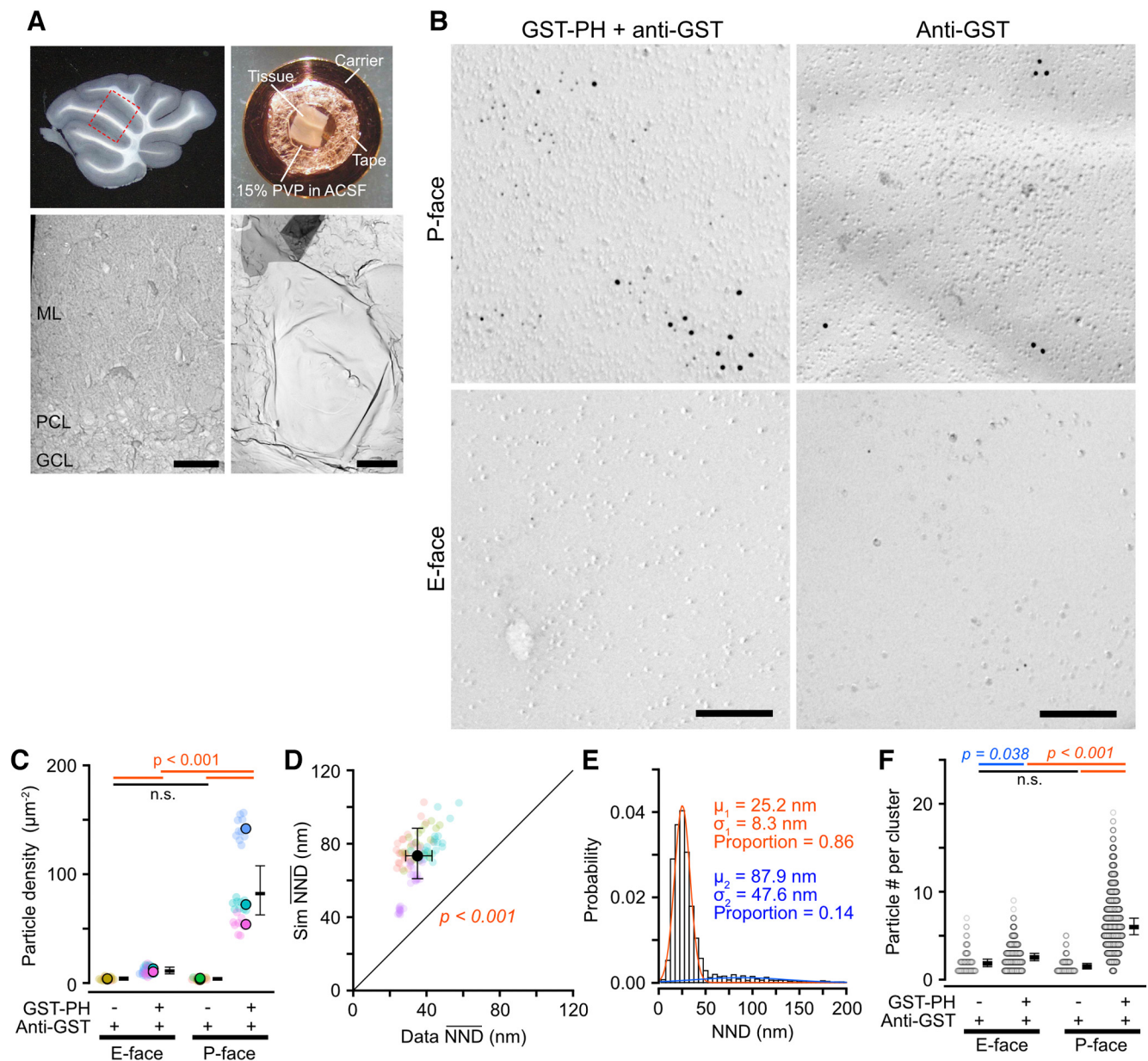
Figure 2. SDS-FRL of PI(4,5)P2 on somatic membranes of Purkinje cells in mouse cerebellum. **A,** Acute cerebellar slice preparation for high-pressure freezing (HPF) and replica preparation. Left-top, An acute sagittal slice of the mouse cerebellum. The dashed line indicates the trimmed region for HPF. Right-top, A trimmed cerebellar slice on a copper carrier with double-sided tape for HPF. Left-bottom, Low-magnification TEM image of the mouse cerebellar replica containing granule cell layer (GCL), Purkinje cell layer (PCL), and molecular layer (ML). Scale bar = 20 μm. Right-bottom, Example TEM image of the somatic membrane of a PC. Scale bar = 5 μm. **B,** Example TEM image of 5-nm gold particle labeling for PI(4,5)P$_2$ with (left) or without (right) GST-PH on P- (top) and E-face (bottom) of the PC somatic membranes of cerebellar PC. Ca$_V$2.1 was co-labeled with 12-nm gold particles. Scale bar = 200 nm. **C,** Statistical comparison of the PI(4,5)P$_2$ particle density on the E-face and P-face of the PC somatic membranes. Closed and transparent circles indicate the means of the PI(4,5)P$_2$ particle density in each cell and each image, respectively, with colors indicating different cells. Black horizontal bars and error bars indicate the emmeans and 95% CIs of the density, respectively. The PI(4,5)P$_2$ density was significantly higher on the P-face than on the E-face of the PC somatic membranes (P-face: 51.2 ± 8.5 particles/μm^2, E-face: 8.0 ± 1.2 particles/μm^2, $n = 213$ images/12 cells/4 mice, $p < 0.001$, Chi-LRT). **D,** Comparison of NND between real (Data NND, x-axis) and simulated (Sim NND, y-axis) PI(4,5)P$_2$ particles on PC somatic membranes. Data-NNDs are significantly smaller than Sim NNDs (Data: 35.1 ± 3.6 nm, Sim: 73.3 ± 7.0 nm, $n = 206$ images/11 cells/4 mice, $p < 0.001$, Chi-LRT). **E,** Distribution of NNDs of the PI(4,5)P$_2$ particles obtained from a single PC somatic membrane ($n = 2,929$ particles). Red and blue lines indicate the distinct components of the NND distribution estimated from the Gaussian mixture modeling. μ, means; σ, standard deviation. **F,** Statistical comparison of the number of 5-nm gold particles per cluster on the PC somatic membranes. The particle clusters were detected using Ward Linkage hierarchical clustering method. The linkage distance threshold was set as 50 nm, which is nearby the maximum distance for cluster detection on the PC somatic membrane using DBSCAN (Fig. 3; Materials and Methods). The particle number per cluster without GST-PH was significantly lower than that with GST-PH in both faces (multiple comparisons with BH method), suggesting that the particle clusters observed on the somatic membranes are mainly due to clustering of PI(4,5)P$_2$ but not to nonspecific aggregation of the primary and secondary antibodies. n.s., not significant.

particle distribution ($n = 49$ images from four cells; observed: 27.8 ± 0.57 nm, simulation: 33.2 ± 0.68 nm; likelihood ratio χ^2 test (Chi-LRT): $p < 0.001$; Fig. 1I), indicating that PI(4,5)P$_2$ forms clusters, rather than randomly distributed, on the HEK293 cell membranes.

Nanoscale PI(4,5)P$_2$ distribution on replica preparations of mouse brain tissues

To visualize the 2D distribution of PI(4,5)P$_2$ on neuronal cell membranes, we labeled PI(4,5)P$_2$ in the mouse cerebellum using SDS-FRL with GST-PH. Acute slices were prepared at
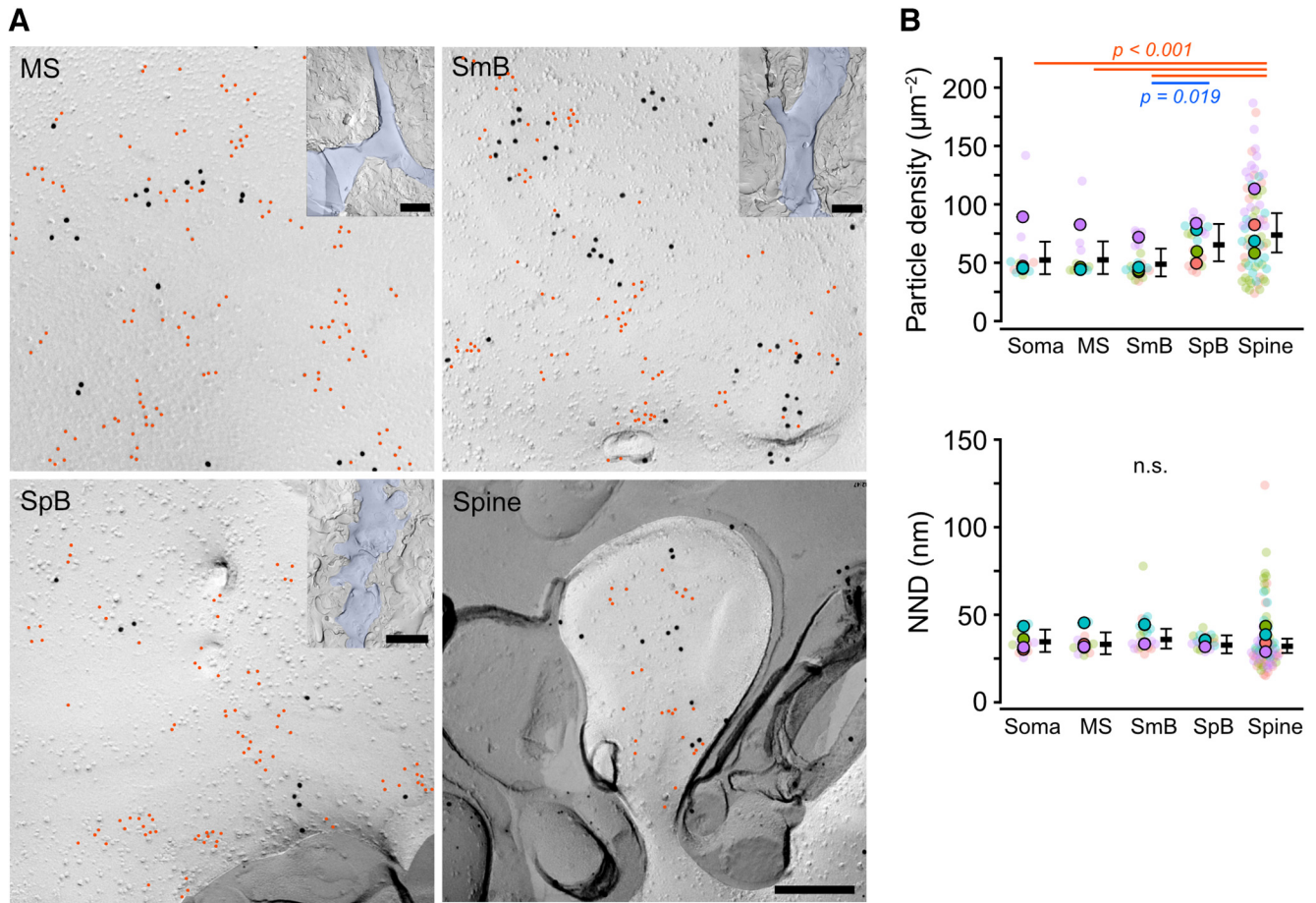
Figure 3. PI(4,5)P$_2$ particle distribution on somatodendritic membranes of PCs. ***A***, Example images of PI(4,5)P$_2$ labeling (red) with Ca$_V$2.1 (black) on the different compartments of PC dendritic membranes: main shaft (MS; top-left), smooth branchlet (SmB; top-right), spiny branchlet (SpB; bottom-left), and spine (bottom-right). Scale bar = 200 nm. Inset, Low-magnification images of MS, SmB, and SpB, respectively, indicated with blue. Red indicates PI(4,5)P$_2$ particles. Scale bars = 2 μm (main panels) and 5 μm (insets). ***B***, Comparison of the PI(4,5)P$_2$ particle density (top) and NNDs (bottom) in the somatodendritic membrane compartments of PCs. Closed and transparent circles indicate the mean values in each animal and cell, respectively, with colors indicating different animals. Black horizontal bars and error bars indicate the emmeans and 95% CIs, respectively. The PI(4,5)P$_2$ density gradually increased from soma and proximal dendrites to distal dendritic components (top, n = 611 images/134 components/4 mice, p < 0.001, Chi-LRT), whereas no significant difference (n.s.) in NNDs was detected between these compartments (bottom, n = 67,380 values/134 components/4 mice, p = 0.49, Chi-LRT). See also Table 2.

Table 2. PI(4,5)P$_2$ distribution in somatodendritic membrane compartments of PCs in mouse cerebellum

Compartment	Mean	SEM	95% CI		*p*-value/*z*-score				
			Lower	Upper	Spine	SpB	SmB	MS	Soma
Particle density (μm^2)									
Soma	52.3	7.0	40.2	68.1	<0.001	0.341	0.949	1.000	—
MS	52.3	7.1	40.2	68.2	<0.001	0.346	0.949	—	−0.002
SmB	48.7	6.0	38.2	62.1	<0.001	0.019	—	0.732	0.732
SpB	62.7	7.8	49.2	80.0	0.149	—	−3.059	−1.848	−1.858
Spine	73.7	8.6	58.6	92.5	—	−2.287	−5.882	−3.917	−3.917
NND (nm)									
Soma	34.3	2.3	30.2	39.0	0.877	1.000	0.871	0.992	—
MS	33.5	2.3	29.3	38.4	0.983	0.994	0.662	—	0.444
SmB	35.9	2.3	31.6	40.8	0.419	0.755	—	−1.347	−0.964
SpB	34.2	2.1	30.3	38.6	0.873	—	1.195	−0.416	0.089
Spine	32.4	2.4	28.0	37.6	—	0.960	1.724	0.544	0.950

MS, main shaft; SmB, smooth branchlet; SpB, spiny branchlet; mean and SEM, marginal means and standard error of means estimated by generalized mixed-effects models; CI, confidential interval; *p*-value, *p*-values obtained using multiple comparison with Tukey method.

physiological temperature to maintain the neuronal condition as intact as possible (Eguchi et al., 2020), and then frozen under high pressure with 15% PVP as a cryoprotectant (Fig. 2A) to minimize damage caused by ice crystals during freezing (Borges-Merjane et al., 2020). After the SDS-digestion to

remove cytosolic proteins and extracellular matrix, cerebellar replicas were sequentially incubated with GST-PH, primary antibodies for GST, and gold particle-conjugated secondary antibodies. Ca$_V$2.1 was co-labeled using an antibody against its intracellular domain (Althof et al., 2015), giving specific

labeling on the P-face of neuronal cell membranes. Immunogold particles labeling PI(4,5)P$_2$ with the GST antibody (PI (4,5)P$_2$ particles) showed significantly higher density on the P-face of the somatic membrane of Purkinje cells (PCs) than on the extracellular leaflets (E-face; Chi-LRT: $p < 0.001$; Fig. 2B,C), indicating the dominance of PI(4,5)P$_2$ distribution on the cytoplasmic leaflet of the cell membranes. The particle density without GST-PH was significantly lower on both E- and P-face of the PC somatic membranes than that with GST-PH (Tukey: $p < 0.001$; Fig. 2B,C), indicating that even the low-density PI(4,5)P$_2$ labeling on the E-face is ascribable to GST-PH binding.

To investigate whether PI(4,5)P$_2$ is clustered or randomly distributed on somatic membranes of PCs, we compared the NNDs between the observed and randomly distributed PI(4,5)P$_2$ particles obtained from the Monte Carlo simulation. The mean NNDs of the observed PI (4,5)P$_2$ particles were around half of the simulated one (Chi-LRT: $p < 0.001$; Fig. 2D), indicating clustering of PI(4,5)P$_2$ on the membrane. The distribution of NNDs between PI(4,5)P$_2$ particles obtained from a PC somatic membrane (Fig. 2E) is highly right-skewed (skewness = 3.55). Fitting this distribution with Gaussian mixture modeling shows that the NNDs between PI(4,5)P$_2$ particles are produced from a mixture of short and long NND populations. These results indicate that the PI (4,5)P$_2$ particles on the PC soma has two distinct distribution patterns, clustered and scattered, and that most PI(4,5)P$_2$ particles constitute clusters (Fig. 2E). The PI (4,5)P$_2$ particle clusters were also observed on the E-face of the somatic membrane. The number of particles in a cluster was significantly lower without GST-PH than that with GST-PH on both E- and P-face (Fig. 2F). These results indicate that PI(4,5)P$_2$ forms clusters on both the outer and inner leaflets of the somatic membranes.

PI(4,5)P$_2$ distribution on somatodendritic compartments of PCs

We next investigate whether the distribution of PI(4,5)P$_2$ differs among somatodendritic compartments of PCs: somata, main shafts (MS), smooth branchlets (SmB), spiny branchlets (SpB), and spines. EM pictures of each dendritic component were taken in the molecular layer (ML) divided into proximal (MS), intermediate (SmB) and distal one-third (SpB, spines) of the ML. Gold particles for PI(4,5)P$_2$ were observed throughout all the dendritic compartments (Fig. 3A). The density of PI(4,5)P$_2$ particles was found to increase gradually from the proximal to the distal dendrites (Chi-LRT: $p < 0.001$; Fig. 3B top; Table 2): spine membranes showed a ~1.5 times higher density of PI (4,5)P$_2$ particles than somatic, MS, and SmB membranes
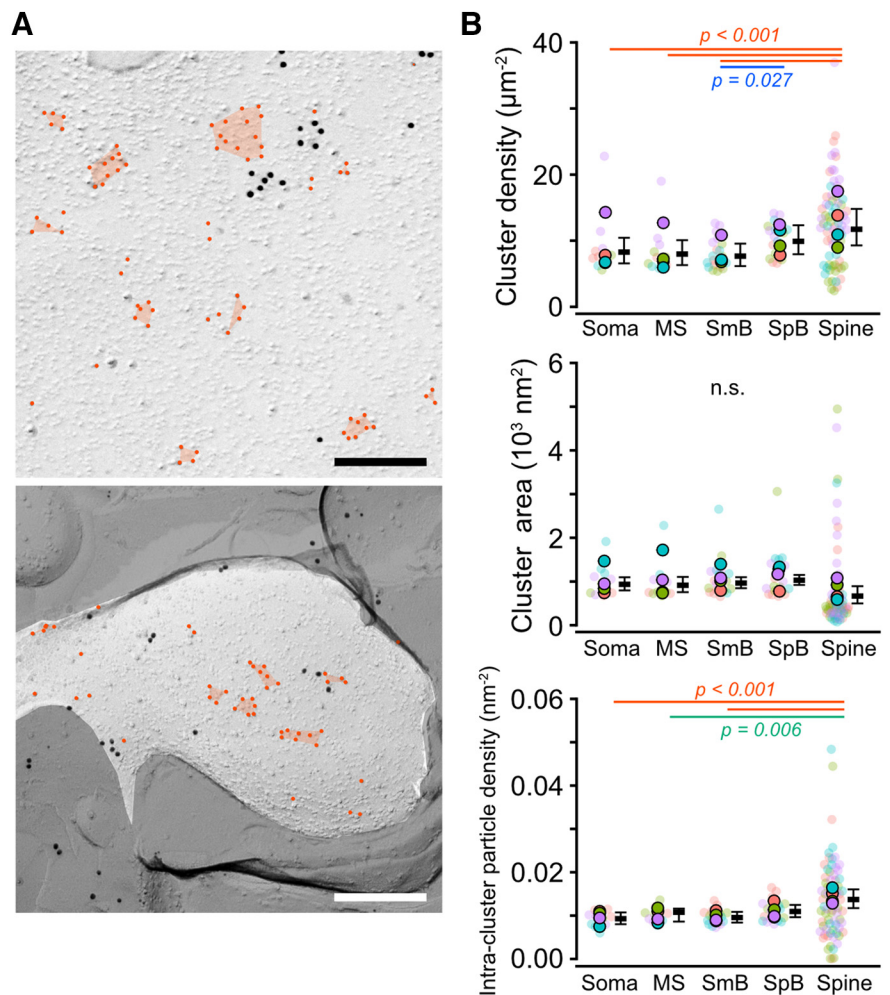
Figure 4. PI(4,5)P$_2$ clustering on the somatodendritic membranes of PCs. **A**, Example images of the PI(4,5)P$_2$ clusters on the somatic (top) and spine (bottom) membrane of PCs. Red circles and polygons indicate PI(4,5)P$_2$ particles and clusters detected by the DBSCAN algorithm, respectively. Scale bars = 200 nm. **B**, Quantitative analysis of the PI(4,5)P$_2$ clusters on the somatodendritic compartments of PCs. Closed and transparent circles indicate the mean values in each animal and cell, respectively, with colors indicating different animals. Black horizontal bars and error bars indicate the emmeans and 95% CIs, respectively. Top, The number of clusters per area (cluster density, $n = 611$ values/134 components/4 mice). Middle, The cluster area (10,479 clusters/124 components/4 mice). Bottom, The intracluster particle density (10,343 clusters/134 components/4 mice). The cluster density and the intracluster particle density are significantly higher in spine membranes compared to the somatic and proximal dendritic membranes ($p < 0.001$, Chi-LRT), whereas there is no significant difference (n.s.) in the cluster area ($p = 0.17$, Chi-LRT). See also Table 3.

(Tukey: $p < 0.001$), whereas no significant difference compared with SpB membranes was detected (Tukey: $p = 0.43$). This result indicates the heterogeneous distribution of PI (4,5)P$_2$ between the somatodendritic compartments of PCs. Mean NNDs of PI(4,5)P$_2$ particles were not significantly different between the compartments (Chi-LRT: $p = 0.55$; Fig. 3B bottom; Table 2), indicating that the local concentration of PI(4,5)P$_2$ does not differ between different somatodendritic compartments of PCs.

Clustering of PI(4,5)P$_2$ on somatodendritic compartments of PCs

The heterogeneous distribution of PI(4,5)P$_2$ between somatodendritic compartments could be caused by the difference in the number, area, or density of the PI(4,5)P$_2$ particle clusters because the PI(4,5)P$_2$ particles on the dendritic membranes formed clusters as seen on the somatic membranes. To test these possibilities, we compared the PI(4,5)P$_2$ cluster profiles (cluster area,

Table 3. PI(4,5)P$_2$ cluster parameters in somatodendritic membrane compartments of PCs in mouse cerebellum

Compartment	Mean	SEM	95% CI		p-value/z-score				
			Lower	Upper	Spine	SpB	SmB	MS	Soma
Cluster density (μm^{-2})									
Soma	8.28	1.00	6.55	10.5	<0.001	0.483	0.859	0.990	—
MS	7.95	0.96	6.27	10.1	<0.001	0.221	0.991	—	0.467
SmB	7.67	0.88	6.13	9.60	<0.001	0.027	—	0.455	0.993
SpB	9.41	1.08	7.51	11.8	0.054	—	−2.943	−2.098	−1.622
Spine	11.7	1.42	9.22	14.8	—	−2.701	−5.321	−4.349	−3.945
Cluster area (nm^2)									
Soma	936	76	798	1098	0.265	0.960	0.999	1.000	—
MS	914	88	757	1105	0.385	0.927	0.991	—	0.185
SmB	965	64	847	1099	0.155	0.992	—	−0.457	−0.288
SpB	1006	68	882	1148	0.085	—	−0.443	−0.812	−0.684
Spine	668	99	500	892	—	2.524	2.270	1.780	2.003
Intracluster particle density (nm^{-2})									
Soma	0.0093	0.0007	0.0080	0.0108	<0.001	0.244	0.996	0.910	—
MS	0.0100	0.0008	0.0086	0.0117	0.006	0.826	0.977	—	−0.865
SmB	0.0096	0.0007	0.0084	0.0109	<0.001	0.319	—	0.588	−0.376
SpB	0.0109	0.0008	0.0095	0.0125	0.055	—	−1.896	−1.063	−2.047
Spine	0.0137	0.0011	0.0117	0.0160	—	−2.693	−4.370	−3.394	−4.308

MS, main shaft; SmB, smooth branchlet; SpB, spiny branchlet; mean and SEM, marginal means and standard error of means estimated by generalized mixed-effects models; CI, confidential interval; p-value, p-values obtained using multiple comparison with Tukey method.

particle number in cluster, and intracluster density) between all compartments of somatodendritic membranes. We detected the clusters using the Density-Based Spatial Clustering of Applications with Noise (DBSCAN) algorithm (Szoboszlay et al., 2017). The DBSCAN detected variable sizes of PI(4,5)P$_2$ particle clusters on the somatodendritic membranes (Fig. 4A). The density of PI(4,5)P$_2$ clusters on the PC cell membranes gradually increased from the proximal to the distal compartments (Chi-LRT: $p < 0.001$; Fig. 4B, top; Table 3); spine membranes showed a higher density of PI(4,5)P$_2$ clusters than somatic, MS, and SmB membranes (Tukey: $p < 0.001$), whereas no significant difference with SpB membranes was detected (Tukey: $p = 0.21$). The cluster area was not significantly different between all compartments of somatodendritic membranes (Chi-LRT: $p = 0.10$; Fig. 4B, middle; Table 3), whereas intracluster PI(4,5)P$_2$ particle density in spines was significantly higher than those in other compartments (Chi-LRT: $p < 0.001$; Fig. 4B, bottom; Table 3). These results suggest that the proximodistal gradient of PI(4,5)P$_2$ along the somatodendritic compartments of PC membranes is ascribable to the differences in the number of PI(4,5)P$_2$ clusters and intracluster PI(4,5)P$_2$ density, rather than the cluster size, between compartments.

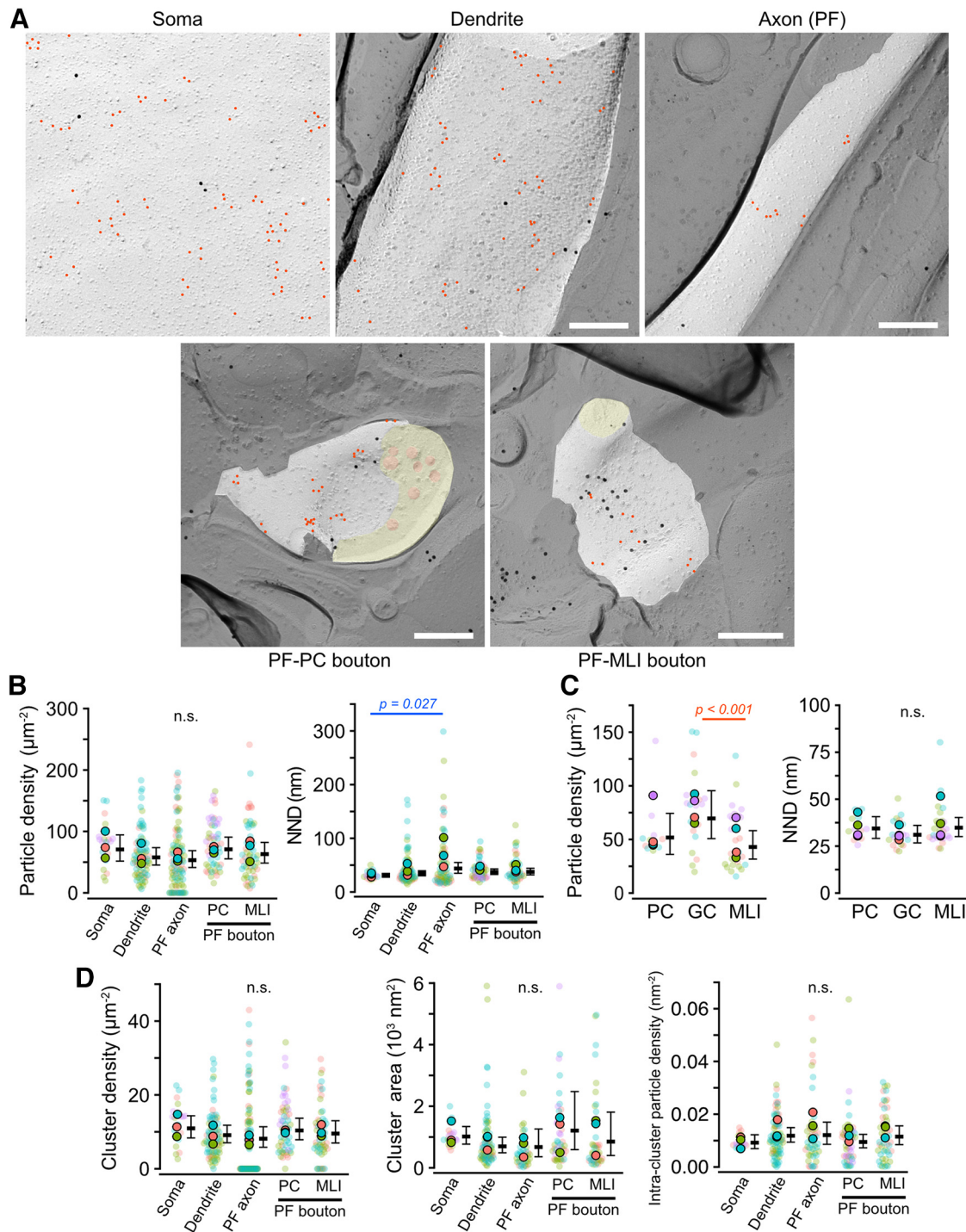**PI(4,5)P$_2$ distribution on membrane compartments of MLIs and GCs**

Next, to examine whether the distribution pattern of PI(4,5)P$_2$ differs between cerebellar neuron types and whether they show heterogeneous distribution between subcellular compartments as observed in PCs, we visualized the PI(4,5)P$_2$ distributions in different compartments of molecular layer interneurons [MLIs; somata, dendrites, presynaptic basket cell boutons on PC somata (BC-PC)] and granule cells [GCs; somata, dendrites, parallel fiber (PF) axons, presynaptic PF boutons with PC spines (PF-PC) or MLI dendrites (PF-MLI)]. Gold particles labeling PI(4,5)P$_2$ were distributed throughout all observed subcellular compartments of GCs and MLIs (Figs. 5A, 6A). In MLIs, the PI(4,5)P$_2$ particle density was not significantly different between the membrane compartments, but the mean NNDs were larger in dendritic and presynaptic bouton membranes

than in somatic membranes (Fig. 5B; Table 4), indicating the higher local PI(4,5)P$_2$ density in the somatic membrane. To further investigate differences in local PI(4,5)P$_2$ density between the compartments, we analyzed parameters of PI(4,5)P$_2$ clusters. The results revealed that the intracluster density of PI(4,5)P$_2$ in the bouton membrane was significantly lower than in other compartments, whereas the cluster density and area were similar (Chi-LRT: $p = 0.43$ and 0.12, respectively; Fig. 5C; Table 4). Histograms of NNDs between PI(4,5)P$_2$ particles were fitted with a Gaussian mixture modeling to obtain the mean NNDs and proportions for the short (clustered) and long (sparse) NND groups, respectively (Fig. 5D). The results show no significant difference in the mean NNDs of both groups between the compartments [Chi-LRT: $p = 0.21$ (short) and 0.12 (long); Fig. 5E], indicating that the difference in mean NND between the MLI compartments is because of the difference of the proportion of the clustered PI(4,5)P$_2$. These results suggest that, in MLI, a higher proportion of PI(4,5)P$_2$ forms denser clusters on the somatic membrane compared with dendritic and presynaptic bouton membranes.

In the GC membranes, the density of PI(4,5)P$_2$ particles was not significantly different between the compartments (Chi-LRT: $p = 0.095$), though the mean NNDs of PI(4,5)P$_2$ particles were slightly but significantly different between somatic and axonal membranes (Tukey: $p = 0.027$; Fig. 6B; Table 5). To examine whether the density of PI(4,5)P$_2$ differs between neuronal cell types in the cerebellum, we compared the PI(4,5)P$_2$ density on the somatic membranes of PCs, GCs, and MLIs. Although the density of PI(4,5)P$_2$ particles in the somatic membrane of GCs was significantly higher than that of MLIs (Tukey: $p < 0.001$), the NNDs of the PI(4,5)P$_2$ particles on somatic membranes of the cerebellar neurons did not differ between the cell types (Chi-LRT: $p = 0.12$; Fig. 6C), indicating a similar local concentration of PI(4,5)P$_2$ in these clusters across the examined cerebellar neuronal cell types. The cluster parameters of PI(4,5)P$_2$ were also not significantly different between the compartments (Fig. 6D; Table 5). These results suggest that PI(4,5)P$_2$ in GC membranes shows a similar distribution pattern throughout the observed subcellular compartments.
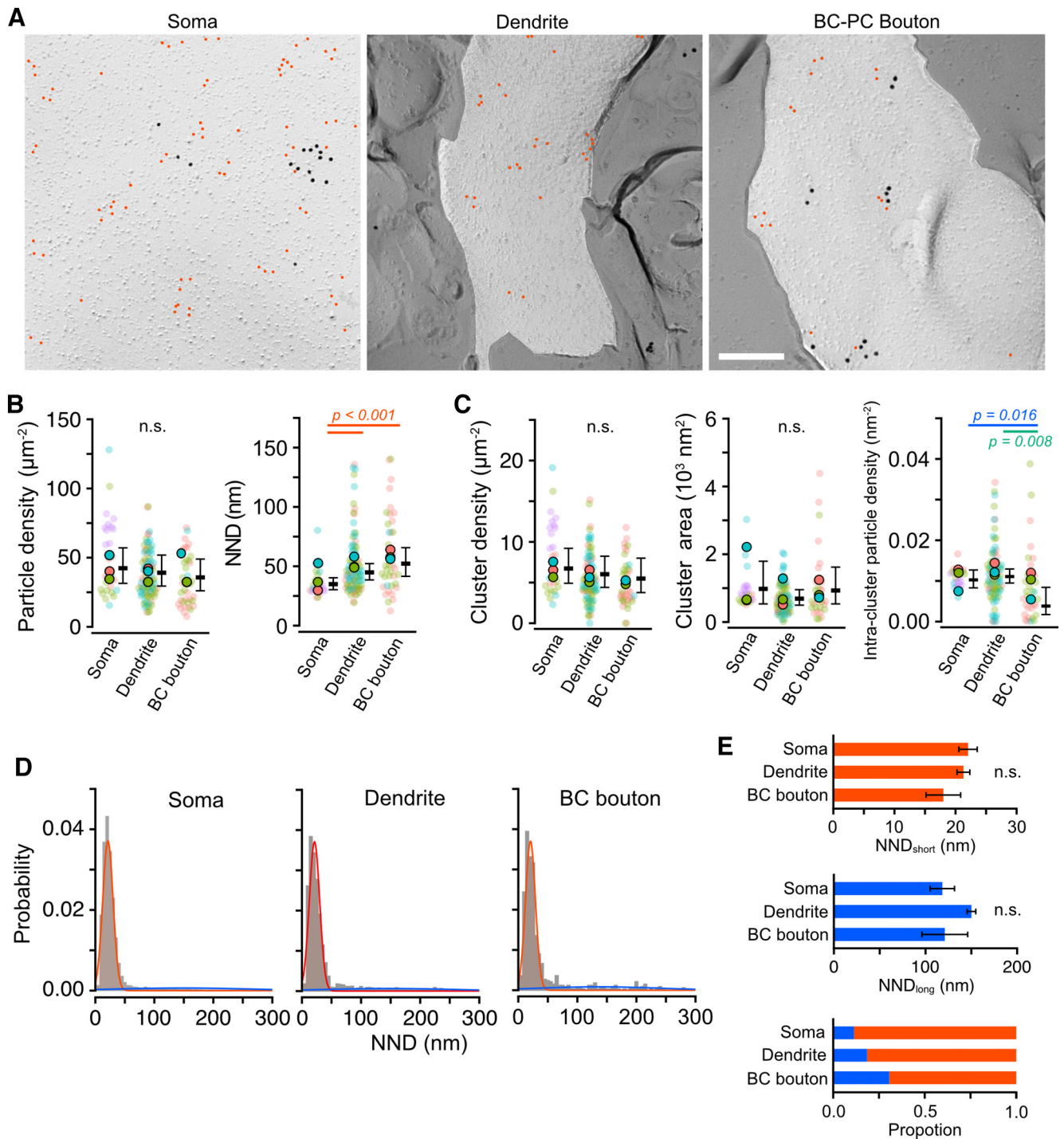
Figure 5. PI(4,5)P$_2$ particle distribution in molecular layer interneuron (MLI) membranes. **A**, Example images obtained from different compartments of MLI membranes: somatic (left), dendrites (middle), and basket cell (BC) presynaptic bouton on PC soma (right). Red indicates PI(4,5)P$_2$ particles. Scale bar = 200 nm. **B**, Comparison of the PI(4,5)P$_2$ particle density (left) and NNDs (right) in different membrane compartments of MLIs. Closed and transparent circles indicate the mean values in each animal and cell, respectively, with colors indicating different animals. Black horizontal bars and error bars indicate the emmeans and 95% CIs, respectively. NNDs in dendritic and BC bouton membranes are significantly larger than that in somatic membranes (n = 24,012 values/152 components/4 mice, $p <$ 0.001, Chi-LRT), whereas there is no significant difference (n.s.) in the density between the compartments (n = 230 images/153 components/4 mice, p = 0.46, Chi-LRT). **C**, Quantitative analysis of the PI(4,5)P$_2$ particle clusters in different MLI membrane compartments. Closed and transparent circles indicate the mean values in each animal and cell, respectively, with colors indicating different animals. Black horizontal bars and error bars indicate the emmeans and 95% CIs, respectively. The intracluster particle density in BC bouton membranes is significantly smaller than the other components (n = 3,766 clusters/149 components/4 mice, p = 0.03, Chi-LRT), whereas no significant difference was detected in the cluster density (n = 230 images/153 components/4 mice, p = 0.43, Chi-LRT) and the cluster area (n = 3,822 clusters/146 components/4 mice, p = 0.12, Chi-LRT) between these compartments. **D**, Distribution of NNDs of the PI(4,5)P$_2$ particles obtained from the somatic (left, n = 20,164 particles), dendritic (middle, n = 3,175 particles), and BC bouton (right, n = 673 particles) membranes of MLIs. Red and blue lines indicate the shorter and longer components of the NND distribution, respectively, estimated from the Gaussian mixture modeling. **E**, Mean values of shorter (red, top) and longer (blue, middle) components of the NND of PI(4,5)P$_2$ particles and their proportion (bottom) on MLI compartments estimated by the Gaussian mixture modeling. Since there are no significant differences in the mean values of both shorter and longer components of the NND (p = 0.21 and 0.24, respectively, Chi-LRT), the higher mean NND values in the dendritic and BC bouton membranes compared to the somatic membranes (Fig. 5B) are ascribable to larger proportions of the scattered PI(4,5)P$_2$ particles in these compartments. See also Table 4.

Figure 6. PI(4,5)P$_2$ particle distribution in cerebellar granule cell (GC) membranes. **A**, Example images obtained from the different compartments of GC membranes: soma (top-left), dendrites (top-middle), parallel fiber (PF) axons (top-right), presynaptic PF boutons on the PC spine (PC-PF, bottom-left), and on the MLI dendrite (PF-MLI, bottom-right). Red indicates PI(4,5)P$_2$ particles. Yellow and orange in the PF boutons indicate the cross-fracture and synaptic vesicle membranes, respectively. Scale bars = 200 nm. **B**, Comparison of the PI(4,5)P$_2$ particle density (left) and NNDs (right) in the different GC membrane compartments. Closed and transparent circles indicate the mean values in each animal and cell, respectively, with colors indicating different animals. Black horizontal bars and error bars indicate the emmeans and 95% CIs, respectively. NNDs show significant differences between the compartments ($n = 67,380$ values/134 components/4 mice, $p < 0.001$, Chi-LRT), whereas there is no significance (n.s.) in the density ($n = 376$ images/320 components/4 mice, $p = 0.09$, Chi-LRT). **C**, Comparison of the PI(4,5)P$_2$ distribution in somatic membranes between different neuron types in mouse cerebellum. Left, The PI(4,5)P$_2$ particle density on the somatic membranes (P-face) of different neuronal cell types in the mouse cerebellum (PC: 51.8 ± 9.6 particles/μm^2, GC: 69.8 ± 11.3 particles/μm^2, MLI: 42.9 ± 6.7 particles/μm^2, $n = 273$ images/57 cells/4 mice, $p = 0.003$, Chi-LRT). Right, NND of the PI(4,5)P$_2$ particles on the somatic membranes of different neuronal cell types in the mouse cerebellum (PC: 34.4 ± 3.0 nm, GC: 31.0 ± 2.4 nm, MLI: 34.8 ± 2.6 nm, $n = 65,607$ values/ 57 cells/4 mice, $p = 0.12$, Chi-LRT). **D**, Quantitative analysis of the PI(4,5)P$_2$ particle clusters in different GC membrane compartments. Closed and transparent circles indicate the mean values in each animal and cell, respectively, with colors indicating different animals. Black horizontal bars and error bars indicate the emmeans and 95% CIs, respectively. There are no significant differences in the cluster density ($n = 376$ images/320 components/4 mice, $p = 0.37$, Chi-LRT), the cluster area ($n = 4070$ clusters/254 components/4 mice, $p = 0.18$, Chi-LRT), and the intracluster particle density ($n = 4004$ clusters/253 compartments/4 mice, $p = 0.50$, Chi-LRT). See also Table 5.

Table 4. PI(4,5)P$_2$ distribution in different membrane compartments of MLIs in mouse cerebellum

Compartment*	Mean**	SEM	95% CI		p-value[†]/z-score		
			Lower	Upper	BC-PC	Dendrite	Soma
Particle density (μm^{-2})							
Soma	42.4	6.5	31.4	57.1	0.449	0.789	—
Dendrite	39.1	5.6	29.5	51.9	0.649	—	0.656
BC-PC bouton	35.7	5.8	26.1	49.0	—	0.887	1.208
NND (nm)							
Soma	34.9	2.6	30.3	40.3	<0.001	<0.001	—
Dendrite	44.9	3.5	38.5	52.2	0.358	—	−3.612
BC-PC bouton	52.2	6.1	41.5	65.7	—	−1.368	−3.650
Cluster density (μm^{-2})							
Soma	6.73	1.08	4.91	9.21	0.417	0.635	—
Dendrite	6.02	0.96	4.40	8.24	0.791	—	0.908
BC-PC bouton	5.49	1.05	3.77	8.00	—	0.652	1.261
Cluster area (nm^2)							
Soma	979	303	534	1794	0.994	0.307	—
Dendrite	690	115	498	955	0.667	—	1.468
BC-PC bouton	931	263	535	1619	—	−0.857	0.109
Intracluster particle density (nm^{-2})							
Soma	0.0103	0.0011	0.0083	0.0127	0.008	0.747	
Dendrite	0.0111	0.0009	0.0095	0.0129	0.016		−0.727
BC-PC bouton	0.0038	0.0015	0.0017	0.0084		2.763	2.975

BC, backet cell; PC, Purkinje cell; mean and SEM, marginal means and standard error of means estimated by generalized mixed-effects models; CI, confidential interval; p-value, p-values obtained using multiple comparison with Tukey method.

Table 5. PI(4,5)P$_2$ distribution in different membrane compartments of GCs in mouse cerebellum

Compartment	Mean	SEM	95% CI		p-value/z-score				
			Lower	Upper	PF-MLI	PF-PC	PF axon	Dendrite	Soma
Particle density (μm^{-2})									
Soma	68.8	10.8	51.6	94.4	0.961	1.000	0.339	0.658	—
Dendrite	57.7	7.2	45.3	73.6	0.916	0.309	0.916	—	1.353
PF axon	53.2	6.9	41.2	68.7	0.540	0.088	—	0.845	1.860
PF-PC bouton	70.9	8.9	55.3	90.7	0.864	—	−2.510	−1.916	−0.108
PF-MLI bouton	63.0	8.5	48.4	82.1	—	0.980	−1.534	−0.847	0.679
NND (nm)									
Soma	30.8	1.8	27.6	34.5	0.153	0.054	0.027	0.521	—
Dendrite	34.5	2.4	30.2	39.4	0.889	0.848	0.298	—	−1.563
PF axon	43.7	5.1	34.8	54.9	0.775	0.726	—	−1.937	−2.944
PF-PC bouton	37.4	2.6	32.7	42.8	1.000	—	1.243	−1.017	−2.701
PF-MLI bouton	37.5	3.1	31.9	44.2	—	−0.023	1.158	−0.922	−2.274
Cluster density (μm^{-2})									
Soma	10.94	1.51	8.35	14.3	0.887	0.994	0.357	0.541	—
Dendrite	9.11	1.20	7.04	11.8	0.997	0.832	0.937	—	1.534
PF axon	8.14	1.39	5.82	11.4	0.885	0.582	—	0.780	1.828
PF-PC bouton	10.37	1.47	7.86	13.7	0.982	—	−1.470	−1.050	0.414
PF-MLI bouton	9.5	1.51	6.99	13.0	—	0.552	−0.931	−0.347	0.926
Cluster area (nm^2)									
Soma	1016	144	770	1340	0.990	0.971	0.772	0.053	—
Dendrite	696	127	488	995	0.974	0.340	1.000	—	2.705
PF axon	673	215	360	1260	0.992	0.749	—	0.091	1.164
PF-PC bouton	1208	442	590	2475	0.869	—	−1.205	−1.859	−0.924
PF-MLI bouton	851	327	400	1808	—	0.969	−0.439	−0.610	0.558
Intracluster particle density (nm^{-2})									
Soma	0.0092	0.0009	0.0077	0.0110	0.989	0.991	0.993	0.119	—
Dendrite	0.0123	0.0017	0.0094	0.0160	0.845	0.370	0.703	—	−2.385
PF axon	0.0082	0.0022	0.0048	0.0139	0.976	1.000	—	1.281	0.432
PF-PC bouton	0.0086	0.0014	0.0063	0.0117	0.968	—	−0.163	1.807	0.455
PF-MLI bouton	0.0101	0.0023	0.0065	0.0157	—	−0.642	−0.593	1.023	−0.480

PF, parallel fiber; PC, Purkinje cell; MLI, molecular layer interneuron; mean and SEM, marginal means and standard error of means estimated by generalized mixed-effects models; CI, confidential interval; p-value, p-values obtained using multiple comparison with Tukey method.
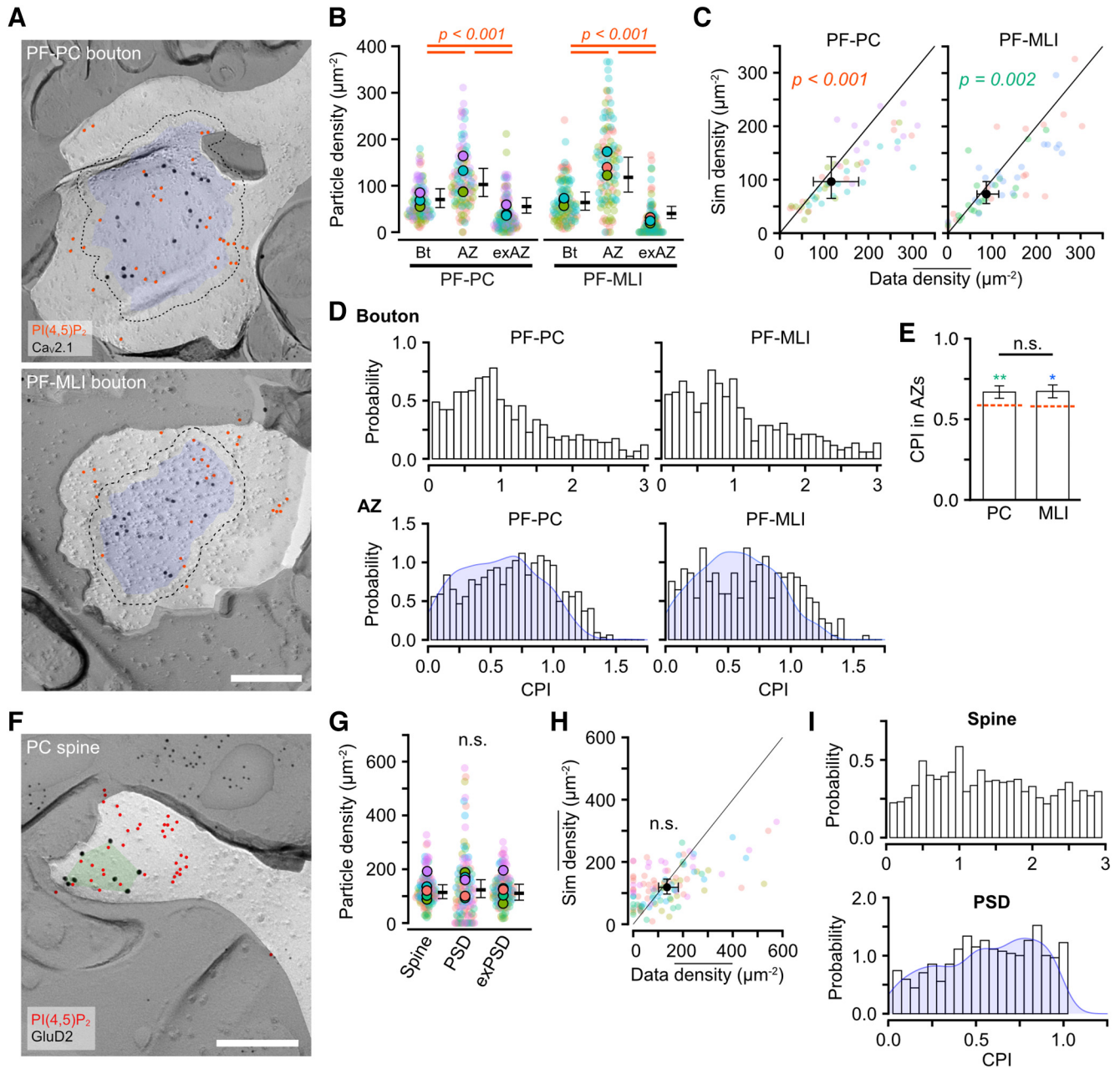
Figure 7. PI(4,5)P$_2$ distribution in presynaptic and postsynaptic membranes of PF-PC synapses. **A**, Example images for PI(4,5)P$_2$ particle distribution on the membranes of PF-PC (top) and PF-MLI bouton (bottom). Red and black circles indicate gold particles for PI(4,5)P$_2$ and Ca$_V$2.1, respectively. The Blue area and dotted line indicate AZ and outer-rim (30 nm from the edge of AZ; Materials and Methods), respectively. Scale bar = 200 nm. **B**, Beeswarm plot of the PI(4,5)P$_2$ density in the whole bouton (Bt), AZs, and extra-AZ region (exAZ) of the PF-PC (left) and PF-MLI (right) bouton membranes. Closed and transparent circles indicate the mean values in each animal and bouton, respectively, with colors indicating different animals. Black horizontal bars and error bars indicate the emmeans and 95% CIs, respectively. The PI(4,5)P$_2$ density was significantly higher in AZs than in the whole bouton and the exAZ in both PF-PC and PF-MLI boutons ($n = 111$ boutons/4 mice, $p < 0.001$, Tukey method). **C**, Comparison of the PI(4,5)P$_2$ density in the AZs between real and simulated random distribution on the PF bouton membranes. Transparent circles indicate the mean densities of each AZ with colors indicating different animals. Black circle and error bars indicate the emmeans and 95% CIs, respectively. The density of the real particle distribution was significantly higher than that of the simulated one in both PF-PC (real: 97.2 ± 19.7 particles/μm^2, sim: 66.7 ± 13.5 particles/μm^2, $n = 55$ boutons/4 mice, $p < 0.001$, Chi-LRT) and PF-MLI (real 86.7 ± 12.4 particles/μm^2, sim: 73.2 ± 10.4 particles/μm^2, $n = 56$ boutons/4 mice, $p = 0.002$, Chi-LRT) AZ membranes. **D**, Distribution of center-periphery index (CPI) of PI(4,5)P$_2$ particles in boutons (top) and AZs (bottom). Blue in the bottom graph indicates the CPI distribution of the simulated particles that are randomly distributed in AZs. **E**, Comparison of CPIs of the PI(4,5)P$_2$ particles in PF-PC and PF-MLI AZs. There is no significant difference in the CPIs between PF-PC and PF-MLI AZs (PF-PC: 0.67 ± 0.02, PF-MLI: 0.67 ± 0.02, $n = 107$ boutons/4 mice, $p = 0.999$, Chi-LRT). Dashed lines with red show the mean CPIs of the simulated randomly-distributed particles. Asterisks on the bars indicate statistical differences in CPIs between real and simulated particles (PF-PC: 0.59 ± 0.02, PF-MLI: 0.58 ± 0.02, $^*p < 0.05$, $^{**}p < 0.01$, Tukey method). **F**, An example image of the PI(4,5)P$_2$ particle distribution on the PC spine membrane. Red and black circles indicate PI(4,5)P$_2$ and GluD2, respectively. The green area indicates postsynaptic density (PSD) based on the cluster of GluD2. Scale bar = 200 nm. **G**, Beeswarm plot of the PI(4,5)P$_2$ density in the whole spine (spine), PSD, and extra-PSD region (exPSD) of the PC spine membranes. Closed and transparent circles indicate the mean values in each animal and spine, respectively, with colors indicating different animals. Black horizontal bars and error bars indicate the emmeans and 95% CIs, respectively. No significant difference (n.s.) in the density was detected between these compartments ($n = 108$ spines/6 mice, $p = 0.77$, Chi-LRT). **H**, Comparison of the PI(4,5)P$_2$ density in the PSDs between real and simulated random distribution on the PC spine membranes. Transparent circles indicate the mean densities of each PSD with colors indicating different animals. Black circle and error bars indicate the emmeans and 95% CIs, respectively. The density of the real and simulated particle distribution was not significantly different (real: 0.59 ± 0.01, sim: 0.55 ± 0.01, $n = 108$ spines/6 mice, $p = 0.25$, Chi-LRT). **I**, Distribution of CPIs of PI(4,5)P$_2$ particles in spines (top) and PSDs (bottom). Blue in the bottom graph indicates the CPI distribution of the simulated particles that are randomly distributed in PSDs. The CPI of the PI(4,5)P$_2$ particles is uniformly distributed in the spines and PSDs, suggesting the random distribution of PI(4,5)P$_2$. See also Table 6.

Table 6. PI(4,5)P$_2$ particle density in synaptic membranes of mouse cerebellar neurons (particles/μm^2)

Compartment	Mean	SEM	95% CI		p-value/z-score		
			Lower	Upper	exAZ	AZ	Bouton
PF-PC boutons							
Bouton	70.2	10.2	52.9	93.3	<0.001	<0.001	—
AZ	102.6	15.2	76.7	137.2	<0.001	—	−5.908
exAZ	55.1	8.3	40.9	74.1	—	6.952	4.018
PF-MLI boutons							
Bouton	63.8	9.9	47.2	86.4	<0.001	<0.001	—
AZ	118.0	18.9	86.2	161.3	<0.001	—	−8.089
exAZ	40.3	6.6	29.2	55.6	—	6.952	5.950
PC spines							
Spine	114.0	12.9	91.0	142	0.749	0.840	—
PSD	124.0	16.5	95.6	161	0.805	—	−0.564
exPSD	111.0	14.8	85.0	144	—	0.628	0.724

PF, parallel fiber; PC, Purkinje cell; MLI, molecular layer interneuron; AZ, active zone; ezAZ, extra AZ; PSD, postsynaptic density; exPSD, extra PSD; mean and SEM, marginal means and standard error of means estimated by generalized mixed-effects models; CI, confidential interval; p-value, p-values obtained using multiple comparison with Tukey method.

PI(4,5)P$_2$ distribution on synaptic membranes
Since many presynaptic proteins related to neurotransmitter release contain PI(4,5)P$_2$-binding domains (T.F.J. Martin, 2001), PI(4,5)P$_2$ is expected to be localized at the presynaptic active zones (AZs). To address this question, we focused on the PI(4,5)P$_2$ particle distribution in the presynaptic membrane of PF (Fig. 7A). The PI(4,5)P$_2$ particle density was significantly higher in the AZs than in the whole bouton and extra-AZ membranes at both PF-PC and PF-MLI synapses (Tukey: $p < 0.001$; Fig. 7B; Table 6). The observed density of PI(4,5)P$_2$ particles in AZs was significantly higher than that of randomly distributed PI(4,5)P$_2$ particles on the bouton membrane by Monte-Carlo simulation [Chi-LRT: $p < 0.001$ (PF-PC) and $p = 0.002$ (PF-MLI); Fig. 7C], suggesting the accumulation of the PI(4,5)P$_2$ in the AZ of PF boutons. Next, we examined how the PI(4,5)P$_2$ particles are distributed within the AZs with center-periphery index (CPI), where a CPI of 0 indicates that the particle is at the center of gravity, and a CPI of 1 indicates the particle is at the edge of the AZ (Kleindienst et al., 2020). The histogram of CPI in the bouton membranes demonstrates that the particles are distributed at a high density within the AZ and that the distribution probability decreases with distance from the AZ (Fig. 7D, top), suggesting the PI(4,5)P$_2$ accumulation in the AZ. The CPI distribution within AZs showed higher probability at around CPI = 1.0 compared with that of the random simulation (Fig. 7D, bottom), indicating that PI(4,5)P$_2$ is preferentially located in the periphery of the AZs. The mean CPI of the PI(4,5)P$_2$ particles in AZs was significantly higher than that of randomly distributed particles in both PF-PC and PF-MLI synapses (Chi-LRT: $p < 0.001$; Fig. 7E). These results suggest that the AZ, especially its periphery, is enriched in PI(4,5)P$_2$, regardless of the postsynaptic cell types.

Next, we investigated the PI(4,5)P$_2$ distribution in PSD of dendritic spines. The PI(4,5)P$_2$ particles were distributed throughout the spine membranes (Fig. 7F), and the density in the PSDs was not significantly different compared with the whole spine and extra-PSD membranes (Chi-LRT: $p = 0.77$; Fig. 7G; Table 6). The observed PI(4,5)P$_2$ particle density in PSDs was not significantly higher than that of the particles randomly distributed in the spine (Chi-LRT: $p = 0.25$; Fig. 7H). Furthermore, the CPI of the PI(4,5)P$_2$ particles in the spines was uniformly distributed, and the CPI in the PSDs was similar to that of the simulated particles randomly distributed (Fig. 7I). These results suggest that PI(4,5)P$_2$ is not specifically accumulated in the postsynaptic site of PC dendritic spines.

The association of ion channels and receptors with PI(4,5)P$_2$ on cell membranes of cerebellar neurons
The visualization of PI(4,5)P$_2$ allows us to investigate the physical association of ion channels and neurotransmitter receptors with PI(4,5)P$_2$, which helps to understand the physiological role of PI(4,5)P$_2$ on neuronal functions. We examined whether these membrane proteins associate with PI(4,5)P$_2$ on cell membranes by double labeling in mouse cerebellar neurons.

The association of Ca$_V$2.1 with PI(4,5)P$_2$
Ca$_V$2.1 is an α-subunit of P/Q-type voltage-gated calcium channels and is regulated by PI(4,5)P$_2$ directly or indirectly through Ca$_V$ β-subunit (Suh and Hille, 2008; Suh et al., 2012). Here, we examined whether Ca$_V$2.1 is associated with PI(4,5)P$_2$ in the neuronal membranes by co-immunolabeling of Ca$_V$2.1 with the PI(4,5)P$_2$ labeling. To assess the association, we compared NNDs from Ca$_V$2.1 to PI(4,5)P$_2$ particles (NND$_{C-P}$) between observed and simulated Ca$_V$2.1 particles. To reproduce the Ca$_V$2.1 clustering in the simulation, we performed a fitted simulation of Ca$_V$2.1 particle distribution (Materials and Methods; Luján et al., 2018b; Kleindienst et al., 2020). In PCs, Ca$_V$2.1 was broadly expressed in somatodendritic membranes (Fig. 8A), as previously reported (Indriati et al., 2013). The real values of NND$_{C-P}$ in somatic, SpB, and spine membranes were significantly shorter than the values obtained with the simulated Ca$_V$2.1 distribution (Fig. 8B), indicating the association of Ca$_V$2.1 with PI(4,5)P$_2$ on the somatodendritic membranes. The mean NND$_{C-P}$ was not significantly different between the compartments of PC membranes (Fig. 8C). In GCs, Ca$_V$2.1 was highly expressed in somatic and presynaptic AZ membranes (Fig. 8D). The comparison of NND$_{C-P}$ between observed and simulated Ca$_V$2.1 particles showed significant differences in the somatic and PF-PC/MLI AZ membranes (Fig. 8E), indicating the association of Ca$_V$2.1 with PI(4,5)P$_2$. The mean NND$_{C-P}$ values in PF-PC and PF-MLI AZs were not significantly different (Fig. 8F). In MLI, Ca$_V$2.1 was expressed in somatic and presynaptic basket cell (BC)-PC bouton membranes (Fig. 9A). The NND$_{C-P}$ in somatic and BC-PC bouton membranes was significantly shorter than the simulated one (Fig. 9B). The mean NND$_{C-P}$ was not significantly different between the somatic and BC-PC bouton membranes of the MLIs (Fig. 9C). These results suggest the ubiquitous association of Ca$_V$2.1 with PI(4,5)P$_2$ in neuronal cell membranes across various cell types and their compartments.
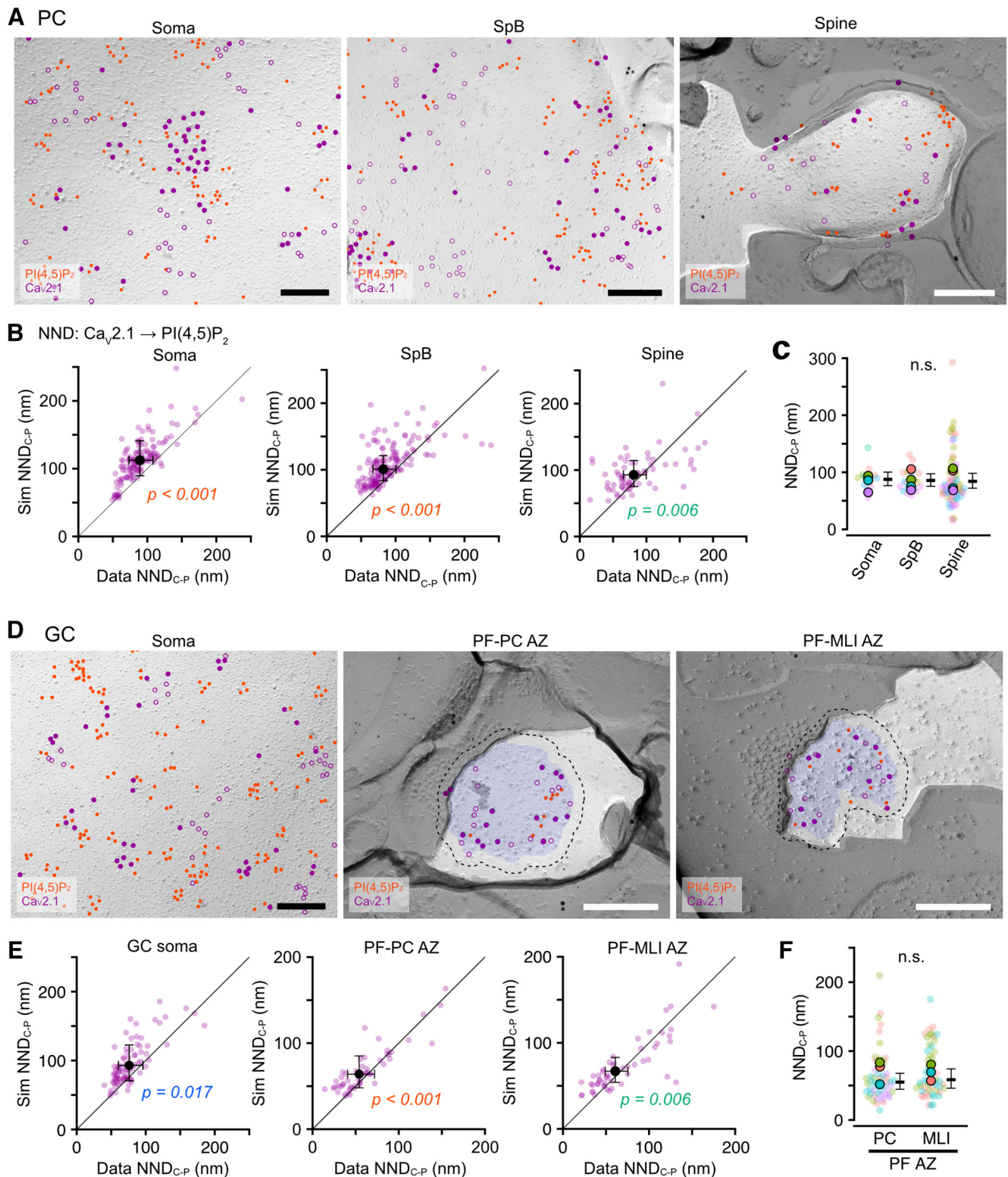
Figure 8. Ubiquitous association of $Ca_V2.1$ with $PI(4,5)P_2$ on cell membranes of PCs and GCs. ***A***, Example images for co-immunolabeling of $PI(4,5)P_2$ and $Ca_V2.1$ on somatic (left), SpB (middle), and spine (right) membranes of the PC. Red and purple (closed, open) circles indicate $PI(4,5)P_2$ and $Ca_V2.1$ (real, fitted-simulated) particles, respectively. Scale bars = 200 nm. ***B***, Comparison of the NNDs from $Ca_V2.1$ to $PI(4,5)P_2$ particles (NND_{C-P}) between real and fitted-simulated $Ca_V2.1$ distribution on somatic (left), SpB (middle), and spine (right) membranes of PCs. The NND_{C-P} of the real distribution was significantly smaller than that of the simulated one in somatic (real: 89.7 ± 9.6 nm, sim: 112.9 ± 12.1 nm, n = 129 images/14 cells/5 mice, $p <$ 0.001, Chi-LRT), SpB (real: 82.3 ± 8.1 nm, sim: 100.5 ± 9.9 nm, n = 158 images/20 dendrites/4 mice, $p <$ 0.001, Chi-LRT), and spine membrane (real: 80.9 ± 8.7 nm, sim: 92.8 ± 9.9 nm, 69 spines/4 mice, p = 0.006, Chi-LRT). ***C***, Comparison of NND_{C-P} between somatodendritic compartments. Closed and transparent circles indicate the mean values in each animal and cell, respectively, with colors indicating different animals. Black horizontal bars and error bars indicate the emmeans and 95% CIs, respectively. There is no significant difference (n.s.) between the PC compartments (n = 12,956 values/92 components/5 mice, p = 0.70, Chi-LRT). ***D***, Example images for co-immunolabeling of $PI(4,5)P_2$ and $Ca_V2.1$ on somatic (left) and presynaptic PF-PC (middle) and PF-MLI (right) AZ membranes of the GC. Red and purple (closed, open) circles indicate $PI(4,5)P_2$ and $Ca_V2.1$ (real, fitted-simulated) particles, respectively. The Blue area and dotted lines indicate AZs and the outer-rim, respectively. Scale bars = 200 nm. ***E***, Comparison of the NND_{C-P} between real and fitted-simulated $Ca_V2.1$ distribution on somatic (left), PF-PC AZ (middle),

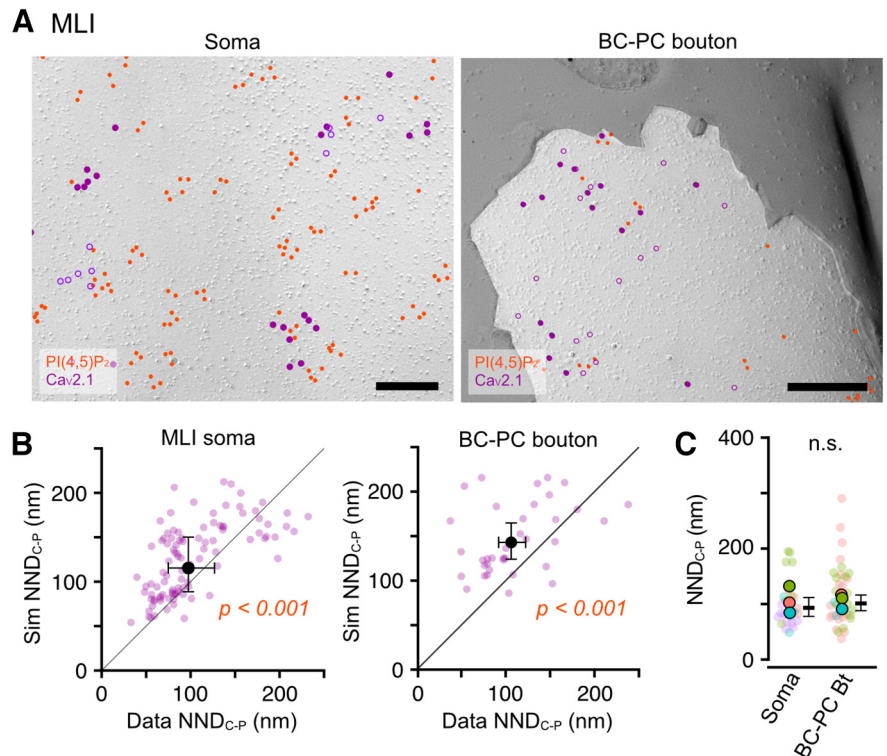*The association of GIRK3 channels with PI(4,5)P$_2$*

G-protein-coupled inwardly rectifying K$^+$ (GIRK) channels are a family of lipid-gated potassium channels that are activated by PI(4,5)P$_2$ and G-protein $\beta\gamma$-subunits (G$_{\beta\gamma}$) released from G-protein coupled receptors (GPCRs; Whorton and MacKinnon, 2011). Thus, GIRK channels are expected to be associated with PI(4,5)P$_2$ to be efficiently activated. To examine whether PI(4,5)P$_2$ and GIRK channels are associated on dendritic membranes of mouse cerebellar PCs, we co-labeled PI(4,5)P$_2$ and GIRK3, the most predominant subunit of GIRK channels in PCs (Aguado et al., 2008; Fernández-Alacid et al., 2009), on the P-face of the dendritic PC membranes. The gold particle labeling GIRK3 (GIRK3 particles) were observed throughout the dendritic SpBs and spines of the PCs (Fig. 10A). We compared the NNDs from GIRK3 to PI(4,5)P$_2$ particles (NND$_{G-P}$) between observed and simulated GIRK3 particles in spines and SpBs spines of PCs. The real NND$_{G-P}$ in both spines and SpBs was significantly shorter than the simulated one (Chi-LRT: $p < 0.001$; Fig. 10B), suggesting that GIRK3 channels are associated with PI(4,5)P$_2$ in the distal dendritic membranes of PCs. GIRK3 channels are also expressed on presynaptic PF boutons, including AZs (Fig. 10A; Fernández-Alacid et al., 2009; Luján et al., 2018b) in PF-PC synapses, and may regulate presynaptic excitability. In the presynaptic AZs, the real NND$_{G-P}$ was significantly shorter than the simulated one (Chi-LRT: $p < 0.001$; Fig. 10B), indicating the association of GIRK3 with PI(4,5)P$_2$. The mean NND$_{G-P}$ in spine and AZ membranes was significantly shorter than that in SpB membranes (Fig. 10C), suggesting the tighter association of GIRK3 and PI(4,5)P$_2$ in synaptic membranes.

The association of mGluR1α with PI(4,5)P$_2$

Group I metabotropic glutamate receptors (mGluRs) are GPCRs coupled with Gα_q subunit and hydrolyze PI(4,5)P$_2$ into inositol 1,4,5-trisphosphate (IP$_3$) and diacylglycerol (DAG) through the activation of PLCβ. A subtype of Group I mGluRs mGluR1α is highly expressed on the dendritic shafts and spines but avoids PSDs in PCs, and forms clusters (L.J. Martin et al., 1992; Mateos

Figure 9. Association of Ca$_V$2.1 with PI(4,5)P$_2$ on cell membranes of MLIs. **A**, Example images for co-immunolabeling of PI(4,5)P$_2$ and Ca$_V$2.1 on somatic (left) and basket cell (BC)-PC bouton (right) membranes of the MLI. Red and purple (closed, open) circles indicate PI(4,5)P$_2$ and Ca$_V$2.1 (real, fitted-simulated) particles, respectively. The P-face of BC-PC boutons were identified based on Ca$_V$2.1 clusters and the surrounding E-face of the PC somatic membranes with Ca$_V$2.1 clusters. Scale bars = 200 nm. **B**, Comparison of the NND$_{C-P}$ between real and fitted-simulated Ca$_V$2.1 distribution on somatic (left) and BC-PC bouton (right) membranes of MLIs. The NND$_{C-P}$ of the real distribution was significantly smaller than that of the simulated one in somatic (real: 97.5 ± 13.1 nm, sim: 115.4 ± 15.5 nm, n = 102 images/26 cells/4 mice, $p < 0.001$, Chi-LRT) and BC-PC bouton membrane (real: 106.0 ± 7.7 nm, sim: 143.0 ± 10.4 nm, 37 boutons/3 mice, $p = 0.006$, Chi-LRT). **C**, Comparison of NND$_{C-P}$ between somatic and bouton membranes. Closed and transparent circles indicate the mean values in each animal and cell, respectively, with colors indicating different animals. Black horizontal bars and error bars indicate the emmeans and 95% CIs, respectively. No significant difference (n.s.) was shown between these compartments (n = 2854 values/63 components/4 mice, $p = 0.29$, Chi-LRT).

et al., 2000; Mansouri et al., 2015; Luján et al., 2018a). To effectively produce the second messengers, PI(4,5)P$_2$ clusters are expected to be located near the mGluR1α cluster on the dendritic membrane of PCs. To address this possibility, we co-labeled mGluR1α with PI(4,5)P$_2$ on the dendritic membranes of PCs and compared the NNDs between mGluR1α and PI(4,5)P$_2$ particles (NND$_{M-P}$) with the fitted simulation of the mGluR1α particle distribution. The mGluR1α particles were distributed as clusters on the membranes of spines and SpBs (Fig. 10D,E) as previously reported (Luján et al., 2018a). The real NND$_{M-P}$ was significantly shorter than the simulated one on the spine membrane (Chi-LRT: $p < 0.001$) but not on the SpB membrane (Chi-LRT: $p = 0.36$; Fig. 10F). These results suggest compartment-specific association of mGluR1α with PI(4,5)P$_2$ on PC spines.

Discussion

To understand the physiological roles of PI(4,5)P$_2$ in neurons, it is essential to know its nanoscale distribution in the neuronal cell membranes. In this study, we examined the global and local density of PI(4,5)P$_2$ using SDS-FRL and revealed that the PI(4,5)P$_2$ density was different between subcellular compartments, rather than between cell types in the cerebellar cortex; in PCs, both of the global and local PI(4,5)P$_2$ densities were higher at the distal

---

and PF-MLI AZ (right) membranes of GCs. The NND$_{C-P}$ of the real distribution was significantly smaller than that of the simulated one in somatic (real: 76.0 ± 9.0 nm, sim: 93.0 ± 13.1 nm, n = 81 images/25 cells/5 mice, $p = 0.017$, Chi-LRT), PF-PC AZ (real: 54.0 ± 7.9 nm, sim: 64.0 ± 9.3 nm, n = 54 AZs/4 mice, $p < 0.001$, Chi-LRT), and PF-MLI AZ membrane (real: 60.8 ± 6.7 nm, sim: 67.0 ± 7.3 nm, 52 AZs/4 mice, $p = 0.006$, Chi-LRT). **F**, Comparison of NND$_{C-P}$ between presynaptic AZs of PF-PC and PF-MLI synapses. Closed and transparent circles indicate the mean values in each animal and AZ, respectively, with colors indicating different animals. Black horizontal bars and error bars indicate the emmeans and 95% CIs, respectively. There is no significant difference in NND$_{C-P}$ between the AZs (n = 1110 values/68 AZs/4 mice, $p = 0.60$, Chi-LRT).
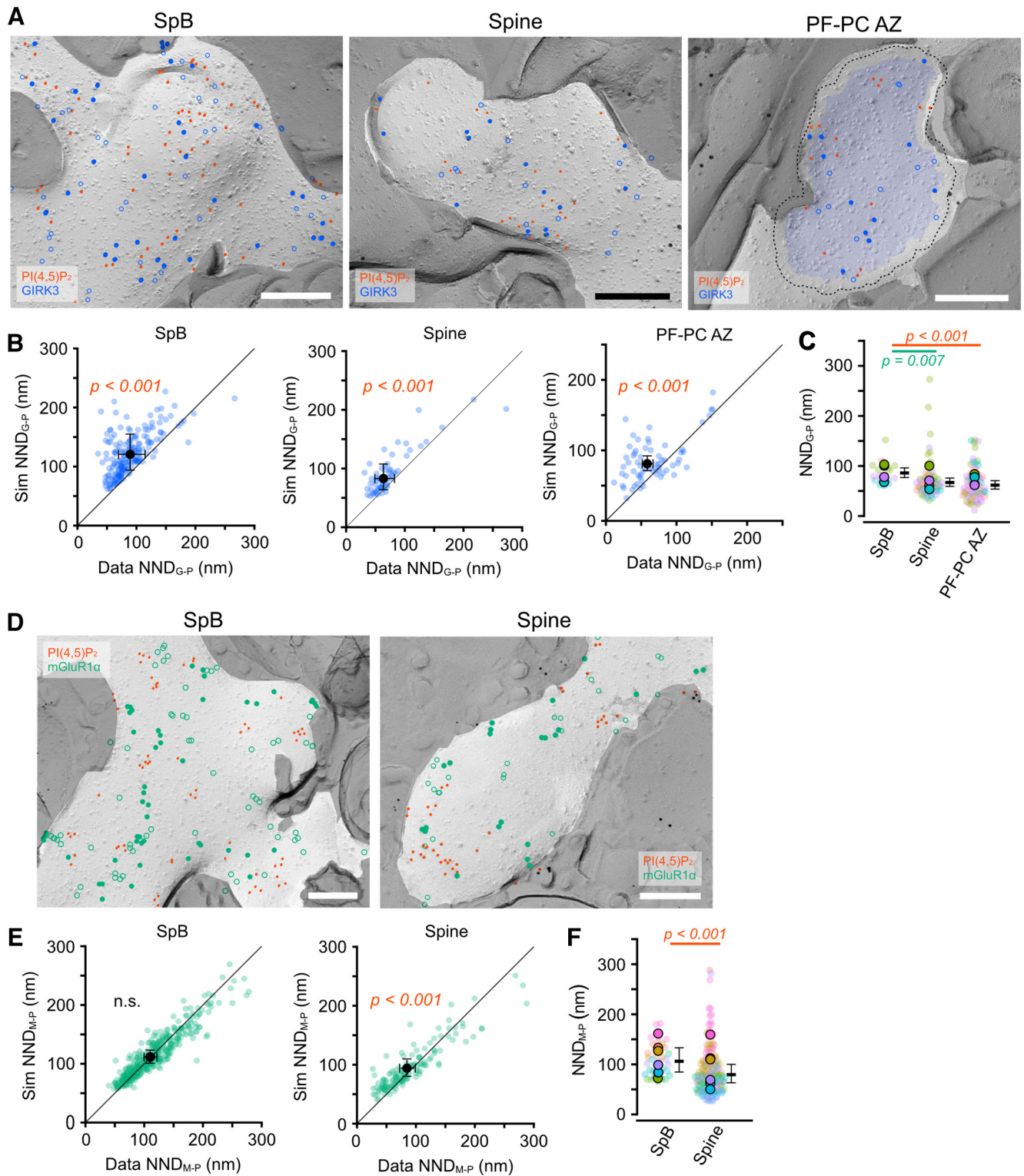
Figure 10. Association of GIRK3 channels and mGluR1α receptors with PI(4,5)P$_2$ on cell membranes of cerebellar neurons. **A**, Example images for co-labeling of PI(4,5)P$_2$ and GIRK3 channels on PC SpB (left), PC spine (middle), and PF-PC AZ (right) membranes. Red and blue (closed, open) circles indicate PI(4,5)P$_2$ and GIRK3 (real, fitted-simulated) particles, respectively. The Blue area and a dotted line on the left indicate the AZ and the outer-rim, respectively. Scale bars = 200 nm. **B**, Comparison of the NNDs from GIRK3 to PI(4,5)P$_2$ particles (NND$_{G-P}$) between real and fitted-simulated GIRK3 distribution on PC SpB (left), PC spine (middle), and PF-PC AZ (right) membranes. The NND$_{G-P}$ of the real distribution was significantly smaller than that of the simulated one in SpB (real: 89.3 ± 11.4 nm, sim: 120.7 ± 15.4 nm, n = 88 images/19 dendrites/5 mice, $p < 0.001$, Chi-LRT), spine (real: 63.6 ± 8.4 nm, sim: 83.0 ± 11.0 nm, n = 57 spines/4 mice, $p < 0.001$, Chi-LRT), and PF-PC AZ membrane (real: 58.6 ± 3.9 nm, sim: 81.1 ± 5.3 nm, 65 AZs/4 mice, $p < 0.001$, Chi-LRT). **C**, Comparison of NND$_{G-P}$ between the postsynaptic and presynaptic compartments of cerebellar neurons. Closed and transparent circles indicate the mean values in each animal and cell, respectively, with colors indicating different animals. Black horizontal bars and error bars indicate the emmeans and 95% CIs, respectively. The NND$_{G-P}$ was significantly shorter in the spine and AZ membranes than in the SpB membrane (4730 values/90 compartments/4 mice, $p < 0.001$, Chi-LRT). **D**, Example images for co-labeling of PI(4,5)P$_2$ and mGluR1α receptors on PC SpB (left) and spine (right) membranes. Red and green (closed, open) circles indicate PI(4,5)P$_2$ and mGluR1α (real, fitted-simulated) particles, respectively. Scale bars = 200 nm. **E**, Comparison of the NNDs from mGluR1α to PI(4,5)P$_2$ particles (NND$_{M-P}$) between real and fitted-simulated mGluR1α distribution on PC SpB (left) and spine (right) membranes. The NND$_{M-P}$ of the real distribution was significantly smaller than that of the simulated

dendrites than at the somatic and proximal dendrites; in GCs, the density was similar at the somata, dendrites, axons, and presynaptic boutons; in MLIs, the density of $PI(4,5)P_2$ in clusters was lower in presynaptic bouton membranes than somatic and dendritic membranes. These heterogeneous $PI(4,5)P_2$ distribution patterns may reflect different roles of $PI(4,5)P_2$ in cell functions between different cell types.

Visualization of $PI(4,5)P_2$ distribution using SDS-FRL

To visualize phospholipids on cell membranes, aldehyde fixation is not suitable because they diffuse laterally even after fixation (K.A.K. Tanaka et al., 2010). The fluorescent protein-tagged $PLC\delta1$-PH has been developed as a specific $PI(4,5)P_2$ probe (Idevall-Hagren and De Camilli, 2015) and enabled single-molecule imaging on the plasma membrane of cultured cells using super-resolution microscopy (Wang and Richards, 2012; Milovanovic et al., 2016). However, in regions with densely packed proteins, e.g., AZs and PSDs, limited accessibility of the probes could hamper the $PI(4,5)P_2$ visualization in brain tissues. Furthermore, the probe competes with endogenous $PI(4,5)P_2$-binding proteins (Suh and Hille, 2008), making it difficult to quantify the $PI(4,5)P_2$ dynamics. Our method solves these problems and is advantageous for visualizing the native $PI(4,5)P_2$ distribution. First, phospholipids are physically immobilized by high-pressure freezing and carbon/platinum replication. In addition, since cytosolic proteins are removed by SDS treatment, $PI(4,5)P_2$ are exposed on the replica surface, making high accessibility of the probe. Although our method has a limited linearity in high density ranges of $PI(4,5)P_2$, the labeling efficiency was constant up to 180 particles/μm^2 (1000 $PI(4,5)P_2/\mu m^2$), covering most of our measurement ranges on neuronal membrane except those within the $PI(4,5)P_2$ clusters.

$PI(4,5)P_2$ makes clusters on neuronal cell membranes in mouse cerebellum

How $PI(4,5)P_2$ is distributed across cell membrane (clustered, randomly, or homogeneously) has been controversial. Previous studies demonstrated that $PI(4,5)P_2$ forms clusters of 50–100 nm in diameter on the cell membrane of PC12 cells (Aoyagi et al., 2005; van den Bogaart et al., 2011; Wang and Richards, 2012) and mouse myoblast cells (Petersen et al., 2016). In contrast, a homogeneous distribution of $PI(4,5)P_2$ on HEK293 cell membranes has been reported (van Rheenen et al., 2005). We found clustering of $PI(4,5)P_2$-labeing particles on the HEK293 cell membrane, and this difference is probably because of the accurate 2D analysis on the replicas, indicating the superiority of our method.

The $PI(4,5)P_2$ cluster area on the neuronal cell membrane was around 1000 nm^2 (corresponding to 35 nm in diameter) in the cerebellar tissues. The mean area of the cluster was almost the same throughout the somatodendritic and axonal membranes and the neuronal cell types. In contrast, the cluster density and the intracluster particle density in the spine membrane are

←

one in the spine membranes (real: 81.8 ± 18.4 nm, sim: 91.2 ± 20.6 nm, n = 140 spines/7 mice, $p < 0.001$, Chi-LRT), but not in the SpB membrane (n = 147 images/35 dendrites/7 mice, p = 0.36, Chi-LRT). **F**, Comparison of NND_{M-P} between the SpB and spine membranes of PCs. Closed and transparent circles indicate the mean values in each animal and cell, respectively, with colors indicating different animals. Black horizontal bars and error bars indicate the emmeans and 95% CIs, respectively. The NND_{M-P} was shorter in the spines than in the SpB membrane (real: 110.0 ± 5.6 nm, sim: 112.0 ± 5.6 nm, n = 22,391 values/140 compartments/7 mice, $p < 0.001$, Chi-LRT). n.s., not significant.

higher than in other somatodendritic compartments of PCs, supporting the contribution of $PI(4,5)P_2$ to spine formation and morphologic long-term plasticity (Ueda and Hayashi, 2013; Lei et al., 2017). Clustering of $PI(4,5)P_2$ indicates the importance of a spatial relationship between the clusters and effector proteins for their effective interaction, as discussed in the following section.

$PI(4,5)P_2$ distribution in the synaptic membrane

We demonstrated the accumulation of $PI(4,5)P_2$ in the AZ of PF boutons, suggesting roles of $PI(4,5)P_2$ on presynaptic activities. Rab3-interacting proteins (RIMs), tethering an SV to the AZ, syntaxin-1A, a member of the SNARE complex, and synaptotagmin-1, a calcium sensor on SVs, have affinity for $PI(4,5)P_2$ (Aoyagi et al., 2005; Honigmann et al., 2013; Milovanovic et al., 2016; de Jong et al., 2018). Since $Ca_V2.1$ directly binds to RIMs, the association of $Ca_V2.1$ with $PI(4,5)P_2$ supports the idea that $PI(4,5)P_2$ anchors Ca^{2+} channels, SVs, and exocytic proteins for fast neurotransmitter release. $PI(4,5)P_2$ also interacts with endocytic proteins, e.g., AP-2, AP180, and dynamin (T.F.J. Martin, 2001; Haucke, 2005; Posor et al., 2015). At calyx of Held synapses in rat brainstem, upregulation of $PI(4,5)P_2$ by the retrograde nitric oxide signals accelerates vesicle endocytosis, which strengthens the homeostatic plasticity to maintain high-frequency synaptic transmission (Eguchi et al., 2012; Taoufiq et al., 2013). $PI(4,5)P_2$ clusters may anchor the proteins involved in this pathway and work as their interaction site.

The association of $PI(4,5)P_2$ and ion channels and receptors

Since $PI(4,5)P_2$ regulates the electrophysiological properties of several ion channels (Suh and Hille, 2008), clarifying spatial relationship between the ion channels and $PI(4,5)P_2$ may provide insight into the regulation mechanism of neuronal excitability. In this study, we found ubiquitous association of Cav2.1 with $PI(4,5)P_2$, not only in the AZ as described above, but also somatodendritic compartments of PCs, GCs and MLIs, indicating that the regulation of Cav2.1 function by $PI(4,5)P_2$ could be extensive. GIRK3 was also ubiquitously associated with $PI(4,5)P_2$ in dendritic membranes of PCs and AZs of PF boutons. Because $PI(4,5)P_2$ is essential to activate GIRK channels by $\beta\gamma$ subunit of G-protein (Whorton and MacKinnon, 2011), the association between GIRK3 and $PI(4,5)P_2$ suggests that GIRK3 is constantly ready to be activated by G-protein coupled receptors. Since GIRK channels are also associated with $GABA_B$ receptors at different compartments of the cerebellar neurons, such as dendritic shafts and spines of PCs and AZs of PF boutons (Fernández-Alacid et al., 2009; Luján et al., 2018b), the co-assembly of $PI(4,5)P_2$, GIRK channels and $GABA_B$ receptors may contribute to effective inhibitory postsynaptic transmission on PCs (Luján et al., 2018b).

In the dendritic shaft and spines of cerebellar PCs, mGluR1α couples with $G\alpha_q$ subunit, $PLC\beta3$ or $\beta4$, and IP$_3$ receptors (IP3Rs) on the smooth endoplasmic reticulum (J. Tanaka et al., 2000; Nakamura et al., 2004; Nomura et al., 2007) to efficiently generate IP$_3$ and DAG from $PI(4,5)P_2$ following glutamate stimulation. However, the spatial correlation of $PI(4,5)P_2$ and mGluR1α was still unclear. We found a significant association of mGluR1α with $PI(4,5)P_2$ on the spine membrane in PCs, which may contribute to the effective production of the IP$_3$/DAG in response to the mGluR1α activation. In contrast, no significant association of mGluR1α with the $PI(4,5)P_2$ was observed in SpBs, though the application of mGluR1 agonist on the dendritic shaft induces calcium release from Ca^{2+} store (Hildebrand et al., 2009). Thus, the tight spatial association of $PI(4,5)P_2$ as observed

for $Ca_V2.1$ and GIRK3 may not be critical for the coupling of mGluR1α activation and intracellular signal cascade depending on the compartments.

The kinetics of IP$_3$ production by mGluR1, Gα_q, and PLCβ have been investigated using caged-IP$_3$ with calcium imaging and mathematical modeling (Finch and Augustine, 1998; Doi et al., 2005; Brown et al., 2008). Finch and Augustine estimated the intraspine IP$_3$ concentration produced by 16 PF stimuli to be 10–20 μM based on the Ca increase induced by cage-IP$_3$ uncaging (Finch and Augustine, 1998), indicating that 600–1200 IP$_3$ is produced in the cytosol of a PC spine (0.1 μm^3, Harris and Stevens, 1988). Mathematical modeling studies have shown that 70 μM (4200 molecules/spine) of IP$_3$ is generated by repetitive PF stimulation (Hernjak et al., 2005; Brown et al., 2008). However, Brown et al., reported that the PI(4,5)P$_2$ of 4000 molecules/μm^2 in the spine membrane, the same as in neuroblastoma cells (Xu et al., 2003), could only produce up to 10 μM IP$_3$, suggesting the requirement of a transient increase in PI(4,5)P$_2$ to 10,000 molecules/μm^2 through stimulus-dependent synthesis (Brown et al., 2008). In our study, since the density of PI(4,5)P$_2$ particles in the spine is 70–100 particles/μm^2, and assuming a labeling efficiency of 17% (Fig. 1D), the amount of PI(4,5)P$_2$ in the spine (1.0 μm^2, Harris and Stevens, 1988) can be estimated to be 400–600 molecules. This density is probably underestimated because the PI(4,5)P$_2$ particles form clusters of $\sim$14,000 particles/μm^2, causing marked reduction of the labeling efficiency. Thus, the amount of PI(4,5)P$_2$ in the spine membrane may be sufficient for the IP$_3$ production elicited by repetitive PF stimulation even in the resting state. Further studies with higher temporal resolution and mathematical modeling will be needed to analyze the precise dynamics of PI(4,5)P$_2$ and IP$_3$ on spine membranes induced by synaptic transmission.

In summary, we could successfully applied SDS-FRL to acute mouse cerebellar slices to analyze the nanoscale two-dimensional distribution of PI(4,5)P$_2$ on the neuronal membrane, and its spatial relationship with GIRK3, Ca$_V$2.1, and mGluR1α in PC dendrites and PF boutons. Notably, we have demonstrated a higher density of PI(4,5)P$_2$ in distal PC dendrites, showing a specific association of mGluR1α with PI(4,5)P$_2$ in spines. PI(4,5)P$_2$ also showed concentration and association with Ca$_V$2.1 and GIRK3 in presynaptic PF AZs. Although the spatial resolution and labeling efficiency at high PI(4,5)P$_2$ densities need to be improved for more accurate quantitative distribution analysis, this method will help to elucidate the physiological role of PI(4,5)P$_2$ in neuronal activity, including synaptic transmission and its long-term plasticity.

References

Aarts E, Verhage M, Veenvliet JV, Dolan CV, Van Der Sluis S (2014) A solution to dependency: using multilevel analysis to accommodate nested data. Nat Neurosci 17:491–496.

Aguado C, Colón J, Ciruela F, Schlaudraff F, Cabañero MJ, Perry C, Watanabe M, Liss B, Wickman K, Luján R (2008) Cell type-specific subunit composition of G protein-gated potassium channels in the cerebellum. J Neurochem 105:497–511.

Aktar S, Takatori S, Tsuji T, Orii M, Ohsaki Y, Cheng J, Fujimoto T (2017) A new electron microscopic method to observe the distribution of phosphatidylinositol 3,4-bisphosphate. Acta Histochem Cytochem 50:141–147.

Althof D, Baehrens D, Watanabe M, Suzuki N, Fakler B, Kulik Á (2015) Inhibitory and excitatory axon terminals share a common nano-architecture of their Cav2.1 (P/Q-type) Ca(2+) channels. Front Cell Neurosci 9:315.

Aoyagi K, Sugaya T, Umeda M, Yamamoto S, Terakawa S, Takahashi M (2005) The activation of exocytotic sites by the formation of phosphatidylinositol 4,5-bisphosphate microdomains at syntaxin clusters. J Biol Chem 280:17346–17352.

Borges-Merjane C, Kim O, Jonas P (2020) Functional electron microscopy, "flash and freeze," of identified cortical synapses in acute brain slices. Neuron 105:992–1006.e6.

Brown S-A, Morgan F, Watras J, Loew LM (2008) Analysis of phosphatidylinositol-4,5-bisphosphate signaling in cerebellar Purkinje spines. Biophys J 95:1795–1812.

Cheng J, Fujita A, Yamamoto H, Tatematsu T, Kakuta S, Obara K, Ohsumi Y, Fujimoto T (2014) Yeast and mammalian autophagosomes exhibit distinct phosphatidylinositol 3-phosphate asymmetries. Nat Commun 5:3207.

de Jong APH, Roggero CM, Ho MR, Wong MY, Brautigam CA, Rizo J, Kaeser PS (2018) RIM C2B domains target presynaptic active zone functions to PIP2-containing membranes. Neuron 98:335–349.e7.

Di Paolo G, De Camilli P (2006) Phosphoinositides in cell regulation and membrane dynamics. Nature 443:651–657.

Doi T, Kuroda S, Michikawa T, Kawato M (2005) Inositol 1,4,5-trisphosphate-dependent Ca2+ threshold dynamics detect spike timing in cerebellar Purkinje cells. J Neurosci 25:950–961.

Eguchi K, Nakanishi S, Takagi H, Taoufiq Z, Takahashi T (2012) Maturation of a PKG-dependent retrograde mechanism for exoendocytic coupling of synaptic vesicles. Neuron 74:517–529.

Eguchi K, Velicky P, Hollergschwandtner E, Itakura M, Fukazawa Y, Danzl JG, Shigemoto R (2020) Advantages of acute brain slices prepared at physiological temperature in the characterization of synaptic functions. Front Cell Neurosci 14:63.

Eguchi K, Montanaro J, Le Monnier E, Shigemoto R (2022) The number and distinct clustering patterns of voltage-gated calcium channels in nerve terminals. Front Neuroanat 16:846615.

Falkenburger BH, Jensen JB, Dickson EJ, Suh BC, Hille B (2010) Phosphoinositides: lipid regulators of membrane proteins. J Physiol 588:3179–3185.

Ferguson KM, Lemmon MA, Schlessinger J, Sigler PB (1995) Structure of the high affinity complex of inositol trisphosphate with a phospholipase C pleckstrin homology domain. Cell 83:1037–1046.

Fernández-Alacid L, Aguado C, Ciruela F, Martín R, Colón J, Cabañero MJ, Gassmann M, Watanabe M, Shigemoto R, Wickman K, Bettler B, Sánchez-Prieto J, Luján R (2009) Subcellular compartment-specific molecular diversity of pre- and post-synaptic GABA-activated GIRK channels in Purkinje cells: pre- and post-synaptic GABAB-activated GIRK channels in Purkinje cells. J Neurochem 110:1363–1376.

Finch EA, Augustine GJ (1998) Local calcium signalling by inositol-1,4,5-trisphosphate in Purkinje cell dendrites. Nature 396:753–756.

Fujita A, Cheng J, Tauchi-Sato K, Takenawa T, Fujimoto T (2009) A distinct pool of phosphatidylinositol 4,5-bisphosphate in caveolae revealed by a nanoscale labeling technique. Proc Natl Acad Sci U S A 106:9256–9261.

Harris KM, Landis DM (1986) Membrane structure at synaptic junctions in area CA1 of the rat hippocampus. Neuroscience 19:857–872.

Harris KM, Stevens JK (1988) Dendritic spines of rat cerebellar Purkinje cells: serial electron microscopy with reference to their biophysical characteristics. J Neurosci 8:4455–4469.

Haucke V (2005) Phosphoinositide regulation of clathrin-mediated endocytosis. Biochem Soc Trans 33:1285–1289.

Hernjak N, Slepchenko BM, Fernald K, Fink CC, Fortin D, Moraru II, Watras J, Loew LM (2005) Modeling and analysis of calcium signaling events leading to long-term depression in cerebellar Purkinje cells. Biophys J 89:3790–3806.

Hildebrand ME, Isope P, Miyazaki T, Nakaya T, Garcia E, Feltz A, Schneider T, Hescheler J, Kano M, Sakimura K, Watanabe M, Dieudonné S, Snutch TP (2009) Functional coupling between mGluR1 and Cav3.1 T-type calcium channels contributes to parallel fiber-induced fast calcium signaling within Purkinje cell dendritic spines. J Neurosci 29:9668–9682.

Honigmann A, van den Bogaart G, Iraheta E, Risselada HJ, Milovanovic D, Mueller V, Müllar S, Diederichsen U, Fasshauer D, Grubmüller H, Hell SW, Eggeling C, Kühnel K, Jahn R (2013) Phosphatidylinositol 4,5-bisphosphate clusters act as molecular beacons for vesicle recruitment. Nat Struct Mol Biol 20:679–686.

Idevall-Hagren O, De Camilli P (2015) Detection and manipulation of phosphoinositides. Biochim Biophys Acta 1851:736–745.

Indriati DW, Kamasawa N, Matsui K, Meredith AL, Watanabe M, Shigemoto R (2013) Quantitative Localization of Cav2.1 (P/Q-Type) Voltage-Dependent Calcium Channels in Purkinje Cells: Somatodendritic

Gradient and Distinct Somatic Coclustering with Calcium-Activated Potassium Channels. J Neurosci 33:3668–3678.

Kleindienst D, Montanaro J, Bhandari P, Case MJ, Fukazawa Y, Shigemoto R (2020) Deep learning-assisted high-throughput analysis of freeze-fracture replica images applied to glutamate receptors and calcium channels at hippocampal synapses. Int J Mol Sci 21:6737.

Konno K, Matsuda K, Nakamoto C, Uchigashima M, Miyazaki T, Yamasaki M, Sakimura K, Yuzaki M, Watanabe M (2014) Enriched expression of GluD1 in higher brain regions and its involvement in parallel fiber–interneuron synapse formation in the cerebellum. J Neurosci 34:7412–7424.

Landis DM, Reese TS (1974) Differences in membrane structure between excitatory and inhibitory synapses in the cerebellar cortex. J Comp Neurol 155:93–125.

Lei W, Myers KR, Rui Y, Hladyshau S, Tsygankov D, Zheng JQ (2017) Phosphoinositide-dependent enrichment of actin monomers in dendritic spines regulates synapse development and plasticity. J Cell Biol 216:2551–2564.

Luján R, Aguado C, Ciruela F, Arus XM, Martín-Belmonte A, Alfaro-Ruiz R, Martínez-Gómez J, de la Ossa L, Watanabe M, Adelman JP, Shigemoto R, Fukazawa Y (2018a) SK2 channels associate with mGlu1α receptors and CaV2.1 channels in Purkinje cells. Front Cell Neurosci 12:311.

Luján R, Aguado C, Ciruela F, Cózar J, Kleindienst D, de la Ossa L, Bettler B, Wickman K, Watanabe M, Shigemoto R, Fukazawa Y (2018b) Differential association of GABAB receptors with their effector ion channels in Purkinje cells. Brain Struct Funct 223:1565–1587.

Maekawa M, Fairn GD (2014) Molecular probes to visualize the location, organization and dynamics of lipids. J Cell Sci 127:4801–4812.

Mansouri M, Kasugai Y, Fukazawa Y, Bertaso F, Raynaud F, Perroy J, Fagni L, Kaufmann WA, Watanabe M, Shigemoto R, Ferraguti F (2015) Distinct subsynaptic localization of type 1 metabotropic glutamate receptors at glutamatergic and GABAergic synapses in the rodent cerebellar cortex. Eur J Neurosci 41:157–167.

Martin TFJ (2001) PI(4,5)P2 regulation of surface membrane traffic. Curr Opin Cell Biol 13:493–499.

Martin LJ, Blackstone CD, Huganir RL, Price DL (1992) Cellular localization of a metabotropic glutamate receptor in rat brain. Neuron 9:259–270.

Masugi-Tokita M, Tarusawa E, Watanabe M, Molnár E, Fujimoto K, Shigemoto R (2007) Number and density of AMPA receptors in individual synapses in the rat cerebellum as revealed by SDS-digested freeze-fracture replica labeling. J Neurosci 27:2135–2144.

Mateos JM, Benítez R, Elezgarai I, Azkue JJ, Lázaro E, Osorio A, Bilbao A, Doñate F, Sarría R, Conquet F, Ferraguti F, Kuhn R, Knöpfel T, Grandes P (2000) Immunolocalization of the mGluR1b splice variant of the metabotropic glutamate receptor 1 at parallel fiber-Purkinje cell synapses in the rat cerebellar cortex. J Neurochem 74:1301–1309.

Milovanovic D, Platen M, Junius M, Diederichsen U, Schaap IAT, Honigmann A, Jahn R, Van Den Bogaart G (2016) Calcium promotes the formation of syntaxin 1 mesoscale domains through phosphatidylinositol 4,5-bisphosphate. J Biol Chem 291:7868–7876.

Nagle JF, Tristram-Nagle S (2000) Structure of lipid bilayers. Biochim Biophys Acta 1469:159–195.

Nakamura M, Sato K, Fukaya M, Araishi K, Aiba A, Kano M, Watanabe M (2004) Signaling complex formation of phospholipase Cbeta4 with metabotropic glutamate receptor type 1alpha and 1,4,5-trisphosphate receptor at the perisynapse and endoplasmic reticulum in the mouse brain. Eur J Neurosci 20:2929–2944.

Nomura S, Fukaya M, Tsujioka T, Wu D, Watanabe M (2007) Phospholipase Cbeta3 is distributed in both somatodendritic and axonal compartments and localized around perisynapse and smooth endoplasmic reticulum in mouse Purkinje cell subsets. Eur J Neurosci 25:659–672.

Ozato-Sakurai N, Fujita A, Fujimoto T (2011) The distribution of phosphatidylinositol 4,5-bisphosphate in acinar cells of rat pancreas revealed with the Freeze-Fracture replica labeling method. PLoS One 6:e23567.

Petersen EN, Chung HW, Nayebosadri A, Hansen SB (2016) Kinetic disruption of lipid rafts is a mechanosensor for phospholipase D. Nat Commun 7:13873.

Posor Y, Eichhorn-Grünig M, Haucke V (2015) Phosphoinositides in endocytosis. Biochim Biophys Acta 1851:794–804.

Schindelin J, Arganda-Carreras I, Frise E, Kaynig V, Longair M, Pietzsch T, Preibisch S, Rueden C, Saalfeld S, Schmid B, Tinevez JY, White DJ, Hartenstein V, Eliceiri K, Tomancak P, Cardona A (2012) Fiji: an open-source platform for biological-image analysis. Nat Methods 9:676–682.

Suh BC, Hille B (2008) PIP2 is a necessary cofactor for ion channel function: how and why? Annu Rev Biophys 37:175–195.

Suh BC, Kim DI, Falkenburger BH, Hille B (2012) Membrane-localized -subunits alter the PIP2 regulation of high-voltage activated Ca2+ channels. Proc Natl Acad Sci U S A 109:3161–3166.

Szoboszlay M, Kirizs T, Nusser Z (2017) Objective quantification of nanoscale protein distributions. Sci Rep 7:15240.

Tabata S, Jevtic M, Kurashige N, Fuchida H, Kido M, Tani K, Zenmyo N, Uchinomiya S, Harada H, Itakura M, Hamachi I, Shigemoto R, Ojida A (2019) Electron microscopic detection of single membrane proteins by a specific chemical labeling. iScience 22:256–268.

Tanaka J, Nakagawa S, Kushiya E, Yamasaki M, Fukaya M, Iwanaga T, Simon MI, Sakimura K, Kano M, Watanabe M (2000) Gq protein alpha subunits Galphaq and Galpha11 are localized at postsynaptic extra-junctional membrane of cerebellar Purkinje cells and hippocampal pyramidal cells. Eur J Neurosci 12:781–792.

Tanaka KAK, Suzuki KGN, Shirai YM, Shibutani ST, Miyahara MSH, Tsuboi H, Yahara M, Yoshimura A, Mayor S, Fujiwara TK, Kusumi A (2010) Membrane molecules mobile even after chemical fixation. Nat Methods 7:865–866.

Taoufiq Z, Eguchi K, Takahashi T (2013) Rho-kinase accelerates synaptic vesicle endocytosis by linking cyclic GMP-dependent protein kinase activity to phosphatidylinositol-4,5-bisphosphate synthesis. J Neurosci 33:12099–12104.

Tóth DJ, Tóth J, Gulyás G, Balla A, Balla T, Hunyady L, Várnai P (2012) Acute depletion of plasma membrane phosphatidylinositol 4,5-bisphosphate impairs specific steps in endocytosis of the G-protein-coupled receptor. J Cell Sci 125:3013–3013.

Tsuji T, Takatori S, Fujimoto T (2019) Definition of phosphoinositide distribution in the nanoscale. Curr Opin Cell Biol 57:33–39.

Ueda Y, Hayashi Y (2013) PIP3 regulates spinule formation in dendritic spines during structural long-term potentiation. J Neurosci 33:11040–11047.

van den Bogaart G, Meyenberg K, Risselada HJ, Amin H, Willig KI, Hubrich BE, Dier M, Hell SW, Grubmüller H, Diederichsen U, Jahn R (2011) Membrane protein sequestering by ionic protein-lipid interactions. Nature 479:552–555.

van Rheenen J, Achame EM, Janssen H, Calafat J, Jalink K (2005) PIP2 signaling in lipid domains: a critical re-evaluation. EMBO J 24:1664–1673.

Wang J, Richards DA (2012) Segregation of PIP2 and PIP3 into distinct nanoscale regions within the plasma membrane. Biol Open 1:857–862.

Wenk MR, De Camilli P (2004) Protein-lipid interactions and phosphoinositide metabolism in membrane traffic: insights from vesicle recycling in nerve terminals. Proc Natl Acad Sci U S A 101:8262–8269.

Whorton MR, MacKinnon R (2011) Crystal structure of the mammalian GIRK2 K+ channel and gating regulation by G proteins, PIP2, and sodium. Cell 147:199–208.

Xu C, Watras J, Loew LM (2003) Kinetic analysis of receptor-activated phosphoinositide turnover. J Cell Biol 161:779–791.

Yu Z, Guindani M, Grieco SF, Chen L, Holmes TC, Xu X (2022) Beyond t test and ANOVA: applications of mixed-effects models for more rigorous statistical analysis in neuroscience research. Neuron 110:21–35.